$B \to X_s l^+ l^-$ in the μ from ν Supersymmetric Standard Model*

Xiao-Jie Hu (胡晓洁)[1,2†] Hai-Bin Zhang (张海斌)[1,2,3‡] Tai-Fu Feng (冯太傅)[1,2,3§]

[1]Department of Physics, Hebei University, Baoding, 071002, China
[2]Hebei Key Laboratory of High-precision Computation and Application of Quantum Field Theory, Baoding, 071002, China
[3]Hebei Research Center of the Basic Discipline for Computational Physics, Baoding, 071002, China

Abstract: We investigate the rare inclusive decay $B \to X_s l^+ l^-$ within the framework of the μ-from-ν Supersymmetric Standard Model ($\mu\nu$SSM), focusing on the origin and phenomenological implications of new-physics effects induced by the model's extended fermion and scalar sectors. We systematically analyze the parameter dependence of the relevant Wilson coefficients and identify the dominant particle sectors responsible for these corrections. Subject to experimental constraints from $\bar{B} \to X_s\gamma$, $B_s^0 \to \mu^+\mu^-$, and the SM-like Higgs boson mass near 125 GeV, we examine the resulting modifications to the branching ratios and forward-backward asymmetries in both low- and high-q^2 regions. Furthermore, by systematically decomposing the interference contributions that govern the forward-backward asymmetry, we demonstrate that the C_7C_{10} and C_9C_{10} interference terms dominate its phenomenological behavior in both kinematic regions.

Keywords: Rare decay, B physics, $\mu\nu$SSM

DOI: **CSTR:**

CPC Accepted

I. INTRODUCTION

Inclusive flavour-changing neutral current (FCNC) rare B decays provide a promising window into physics beyond the Standard Model (SM), as their theoretical predictions are subject to comparatively small uncertainties from non-perturbative QCD effects. The inclusive semileptonic decay $B \to X_s l^+ l^-$ has been extensively studied within the SM, including the dominant perturbative contributions [1], two-loop QCD corrections [2, 3], and $c\bar{c}$ resonance effects [4−6].

In this work, we use the SM prediction for $B \to X_s l^+ l^-$ from Ref. [7]. This calculation includes next-to-next-to-leading-order (NNLO) QCD corrections, next-to-leading-order (NLO) electroweak corrections, and power corrections in the heavy-quark expansion (HQE). Long-distance charmonium contributions are treated using the Krüger-Sehgal (KS) approach, including $\frac{1}{m_c^2}$ corrections. The corresponding SM branching-ratio predictions in the low- and high-q^2 regions are

$$\begin{aligned}&\mathrm{BR}(B \to X_s l^+ l^-)^{\mathrm{SM}}_{q^2\in[1,6]\,\mathrm{GeV}^2} = (1.69 \pm 0.13) \times 10^{-6},\\ &\mathrm{BR}(B \to X_s l^+ l^-)^{\mathrm{SM}}_{q^2\in[14.4,25]\,\mathrm{GeV}^2} = (3.04 \pm 0.69) \times 10^{-7},\ (l = e,\mu).\end{aligned} \tag{1}$$

The decay $B \to X_s l^+ l^-$ is conventionally analyzed in two kinematic regions: the low-q^2 region, $1\,\mathrm{GeV}^2 \le q^2 \le 6\,\mathrm{GeV}^2$, and the high-$q^2$ region, $14.4\,\mathrm{GeV}^2 \le q^2 \le 25\,\mathrm{GeV}^2$, where q^2 denotes the dilepton invariant mass squared. The experimental averages for the branching ratios, obtained as weighted averages of measurements from BaBar [8, 9] and Belle [10, 11], are as follows:

$$\begin{aligned}&\mathrm{BR}(B \to X_s l^+ l^-)^{\mathrm{exp}}_{q^2\in[1,6]\,\mathrm{GeV}^2} = (1.58 \pm 0.37) \times 10^{-6},\\ &\mathrm{BR}(B \to X_s l^+ l^-)^{\mathrm{exp}}_{q^2\in[14.4,25]\,\mathrm{GeV}^2} = (4.8 \pm 1.0) \times 10^{-7},\ (l = e,\mu),\end{aligned} \tag{2}$$

These experimental results are consistent with SM predictions, indicating that precise measurements of B decay processes impose stringent constraints on new physics beyond the SM. The low- and high-q^2 regions exhibit

Received 31 August 2026; Accepted 5 November 2026

* The work has been supported by the National Natural Science Foundation of China (NNSFC) with Grants No. 12235008 and No. 12675001, Hebei Natural Science Foundation with Grant No. A2023201041

† E-mail: xiaojiehu.research@outlook.com
‡ E-mail: hbzhang@hbu.edu.cn
§ E-mail: fengtf@hbu.edu.cn

Content from this work may be used under the terms of the Creative Commons Attribution 3.0 licence. Any further distribution of this work must maintain attribution to the author(s) and the title of the work, journal citation and DOI. Article funded by SCOAP[3] and published under licence by Chinese Physical Society and the Institute of High Energy Physics of the Chinese Academy of Sciences and the Institute of Modern Physics of the Chinese Academy of Sciences and IOP Publishing Ltd

complementary sensitivities to different short-distance Wilson coefficients [12−14]. In particular, the contribution of C_7 and the interference between C_7 and C_9 are more pronounced in the low-q^2 region, whereas C_9 and C_{10} have a greater impact in the high-q^2 region [15, 16]. A separate analysis of these two regions is therefore necessary to assess the kinematic dependence of new-physics effects and to identify how these effects manifest in observables with different sensitivities to the Wilson coefficients. In addition to the branching ratios, the forward-backward asymmetry $A_{\rm FB}$ provides a complementary observable that is sensitive to the structure of new-physics loop contributions.

The updated experimental data on $B \to X_s l^+ l^-$ in the low- and high-q^2 regions are summarized below [11]

$$\begin{aligned} &A_{\rm FB}(B \to X_s l^+ l^-)^{\rm exp}_{q^2\in[1,6]\,{\rm GeV}^2} = 0.30 \pm 0.24 \pm 0.04, \\ &A_{\rm FB}(B \to X_s l^+ l^-)^{\rm exp}_{q^2\in[14.4,25]\,{\rm GeV}^2} = 0.28 \pm 0.15 \pm 0.02. \end{aligned} \tag{3}$$

The corresponding SM predictions are given in [17]

$$\begin{aligned} &A_{\rm FB}(B \to X_s l^+ l^-)^{\rm SM}_{q^2\in[1,6]\,{\rm GeV}^2} = -0.07 \pm 0.04, \\ &A_{\rm FB}(B \to X_s l^+ l^-)^{\rm SM}_{q^2\in[14.4,25]\,{\rm GeV}^2} = 0.40 \pm 0.04. \end{aligned} \tag{4}$$

Owing to the currently sizable experimental uncertainties, the forward-backward asymmetry $A_{\rm FB}$ cannot yet stringently discriminate between the Standard Model (SM) and new-physics effects. Improved experimental precision and larger data samples in future measurements are expected to impose stronger constraints on new physics.

Among the various extensions of the SM, supersymmetric models are well-motivated candidates for new physics. The rare inclusive decay $\bar{B} \to X_s \gamma$ has been computed with higher-order QCD corrections in Refs. [18−23]. The inclusive decay $B \to X_s l^+ l^-$ has been extensively studied within the Two-Higgs Doublet Model (THDM) and the Minimal Supersymmetric Standard Model (MSSM) [24−31]. Phenomenological constraints from the measured $\bar{B} \to X_s \gamma$ and $B \to X_s l^+ l^-$ branching ratios have been discussed in Refs. [13, 32, 33]. Predictions for exclusive and inclusive B-meson semileptonic observables, including branching ratios and forward-backward asymmetries, have been presented in Refs. [14, 34]. Comprehensive reviews of SM-extension effects in B-decay physics can be found in Refs. [35, 36]. Adopting the mass insertion approximation, dedicated parameter constraints from $B \to X_s l^+ l^-$ processes have been derived in Refs. [37, 38].

In contrast to the Minimal Supersymmetric Standard Model [39, 40], the $\mu\nu$SSM [41−43] addresses the μ problem of the MSSM [44] via the R-parity-breaking coupling in the superpotential. When electroweak symmetry is broken, the μ term is generated spontaneously by the nonzero right-handed sneutrino vacuum expectation values (VEVs), $\mu = \lambda_i \langle \tilde{\nu}_i^c \rangle$. Moreover, a TeV-scale seesaw mechanism can generate three small neutrino masses at tree level. The neutrino mass and mixing patterns in the $\mu\nu$SSM have been systematically studied in our previous work [45], and the parameter regions adopted in the present analysis are consistent with those constraints.

In our previous work, we investigated the rare decays $\bar{B} \to X_s \gamma$ and $B_s^0 \to \mu^+ \mu^-$ within the $\mu\nu$SSM framework [46, 47]. In this work, we consider the FCNC process $B \to X_s l^+ l^-$, which provides a complementary probe of the combined effects of the electromagnetic dipole and semileptonic Wilson coefficients C_7, C_9, and C_{10}. Because of the extended fermion and scalar sectors of the $\mu\nu$SSM, the relevant loop amplitudes receive model-dependent contributions through modified couplings and mixing structures. Therefore, beyond the numerical predictions of decay observables, it is essential to identify the origin of these corrections at the Wilson-coefficient level and to clarify how different sectors of the $\mu\nu$SSM govern their parameter dependence. In this paper, we systematically analyze the new-physics contributions to the relevant Wilson coefficients, trace their dependence on the model parameters, and investigate their combined effects on the branching ratios and forward-backward asymmetries in different q^2 regions.

The paper is organized as follows. In Section II, we briefly introduce the $\mu\nu$SSM. In Section III, we present the effective Hamiltonian for $B \to X_s l^+ l^-$. The formulas for the branching ratios and forward-backward asymmetries are given in Section IV. The numerical analysis is presented in Section V. Additional constraints are discussed in Section VI, and Section VII provides a summary.

II. THE $\mu\nu$SSM

Compared with the MSSM, the $\mu\nu$SSM contains three singlet neutrino superfields. The superpotential of the $\mu\nu$SSM is given by [41]

$$\begin{aligned} W = &\epsilon_{ab}\big(Y_{u_{ij}} \hat{H}_u^b \hat{Q}_i^a \hat{u}_j^c + Y_{d_{ij}} \hat{H}_d^a \hat{Q}_i^b \hat{d}_j^c \\ &+ Y_{e_{ij}} \hat{H}_d^a \hat{L}_i^b \hat{e}_j^c + Y_{\nu_{ij}} \hat{H}_u^b \hat{L}_i^a \hat{\nu}_j^c\big) \\ &- \epsilon_{ab} \lambda_i \hat{\nu}_i^c \hat{H}_d^a \hat{H}_u^b + \frac{1}{3} \kappa_{ijk} \hat{\nu}_i^c \hat{\nu}_j^c \hat{\nu}_k^c \,. \end{aligned} \tag{5}$$

Here, $a, b = 1, 2$ denote the $SU(2)$ indices, with the antisymmetric tensor ϵ_{ab}, and $i, j, k = 1, 2, 3$ are generation indices. $\hat{H}_d^T = (\hat{H}_d^0, \hat{H}_d^-)$, $\hat{H}_u^T = (\hat{H}_u^+, \hat{H}_u^0)$, $\hat{Q}_i^T = (\hat{u}_i, \hat{d}_i)$, and $\hat{L}_i^T = (\hat{\nu}_i, \hat{e}_i)$ represent $SU(2)$ doublet superfields, while $\hat{d}_j^c$, $\hat{u}_j^c$, and $\hat{e}_j^c$ denote the singlet down-type, up-type, and charged-lepton superfields, respectively. Moreover, Y, κ, and λ denote dimensionless matrices, a totally symmetric

CPC Accepted

tensor, and a vector, respectively. The last two terms in Eq. (5) explicitly violate lepton number and R-parity. After EWSB, the right-handed sneutrino vacuum expectation values (VEVs) spontaneously generate the effective bilinear terms $\epsilon_{ab}\mu\hat{H}_d^a\hat{H}_u^b$, where μ is defined as $\mu = \lambda_i\langle\tilde{\nu}_i^c\rangle$. In addition, this electroweak symmetry breaking mechanism generates effective Majorana masses for neutrinos through the last term in Eq. (5). In this paper, the summation convention is implied for repeated indices.

Once the electroweak symmetry is spontaneously broken, the neutral scalars generally develop VEVs as follows:

$$\langle H_d^0\rangle = \upsilon_d, \qquad \langle H_u^0\rangle = \upsilon_u, \qquad \langle\tilde{\nu}_i\rangle = \upsilon_{\nu_i}, \qquad \langle\tilde{\nu}_i^c\rangle = \upsilon_{\nu_i^c}. \quad (6)$$

Thus, the neutral scalar fields can be defined as

$$\begin{aligned} H_d^0 &= \frac{h_d + iP_d}{\sqrt{2}} + \upsilon_d, \qquad \tilde{\nu}_i = \frac{(\tilde{\nu}_i)^{\Re} + i(\tilde{\nu}_i)^{\Im}}{\sqrt{2}} + \upsilon_{\nu_i}, \\ H_u^0 &= \frac{h_u + iP_u}{\sqrt{2}} + \upsilon_u, \qquad \tilde{\nu}_i^c = \frac{(\tilde{\nu}_i^c)^{\Re} + i(\tilde{\nu}_i^c)^{\Im}}{\sqrt{2}} + \upsilon_{\nu_i^c}, \end{aligned} \quad (7)$$

and

$$\tan\beta = \frac{\upsilon_u}{\sqrt{\upsilon_d^2 + \upsilon_{\nu_i}\upsilon_{\nu_i}}}. \quad (8)$$

where υ_{ν_i} and $\upsilon_{\nu_i^c}$ denote the VEVs of the left-handed and right-handed sneutrino superfields, respectively. Since $\upsilon_{\nu_i} \ll \upsilon_d, \upsilon_u$, $\tan\beta$ can be defined as usual, with $\tan\beta = \frac{\upsilon_u}{\upsilon_d}$.

In the $\mu\nu$SSM, the general soft SUSY-breaking terms are written as

$$\begin{aligned} -\mathcal{L}_{\rm soft} &= m_{\tilde{Q}_{ij}}^2\tilde{Q}_i^{a*}\tilde{Q}_j^a + m_{\tilde{u}_{ij}^c}^2\tilde{u}_i^{c*}\tilde{u}_j^c + m_{\tilde{d}_{ij}^c}^2\tilde{d}_i^{c*}\tilde{d}_j^c + m_{\tilde{L}_{ij}}^2\tilde{L}_i^{a*}\tilde{L}_j^a \\ &+ m_{\tilde{e}_{ij}^c}^2\tilde{e}_i^{c*}\tilde{e}_j^c + m_{H_d}^2H_d^{a*}H_d^a + m_{H_u}^2H_u^{a*}H_u^a + m_{\tilde{\nu}_{ij}^c}^2\tilde{\nu}_i^{c*}\tilde{\nu}_j^c \\ &+ \epsilon_{ab}\left[(A_uY_u)_{ij}H_u^b\tilde{Q}_i^a\tilde{u}_j^c + (A_dY_d)_{ij}H_d^a\tilde{Q}_i^b\tilde{d}_j^c\right. \\ &\left.+ (A_eY_e)_{ij}H_d^a\tilde{L}_i^b\tilde{e}_j^c + \text{H.c.}\right] \\ &+ \left[\epsilon_{ab}(A_\nu Y_\nu)_{ij}H_u^b\tilde{L}_i^a\tilde{\nu}_j^c - \epsilon_{ab}(A_\lambda\lambda)_i\tilde{\nu}_i^cH_d^aH_u^b\right. \\ &\left.+ \frac{1}{3}(A_\kappa\kappa)_{ijk}\tilde{\nu}_i^c\tilde{\nu}_j^c\tilde{\nu}_k^c + \text{H.c.}\right] \\ &- \frac{1}{2}\left(M_3\tilde{\lambda}_3\tilde{\lambda}_3 + M_2\tilde{\lambda}_2\tilde{\lambda}_2 + M_1\tilde{\lambda}_1\tilde{\lambda}_1 + \text{H.c.}\right). \end{aligned} \quad (9)$$

Here, the first eight terms are mass-squared terms for sleptons, Higgs scalars, and squarks. In the last three terms, the Majorana masses corresponding to the gauginos $\tilde{\lambda}_3$, $\tilde{\lambda}_2$, and $\tilde{\lambda}_1$ are denoted by M_3, M_2, and M_1, respectively. The remaining terms are the trilinear scalar couplings. In addition to the terms from $\mathcal{L}_{\rm soft}$, D-terms and F-terms also contribute to the tree-level scalar potential [42].

The 8×8 mass matrix $M_{S^\pm}^2$ for the charged scalar fields contains the massless, unphysical Goldstone modes $G^\pm$, as described in Refs. [48−50]:

$$G^\pm = \frac{1}{\sqrt{\upsilon_d^2 + \upsilon_u^2 + \upsilon_{\nu_i}\upsilon_{\nu_i}}}\left(\upsilon_dH_d^\pm - \upsilon_uH_u^\pm - \upsilon_{\nu_i}\tilde{e}_{L_i}^\pm\right). \quad (10)$$

In the unitary gauge, the W boson absorbs the Goldstone bosons $G^\pm$, and its squared mass is given by

$$m_W^2 = \frac{e^2}{2s_W^2}\left(\upsilon_u^2 + \upsilon_d^2 + \upsilon_{\nu_i}\upsilon_{\nu_i}\right) \quad (11)$$

Here, e denotes the electromagnetic coupling constant, and s_W is defined as $\sin\theta_W$, where θ_W denotes the Weinberg angle.

III. EFFECTIVE HAMILTONIAN FOR $B \to X_s l^+ l^-$ $(l = e, \mu, \tau)$

The effective Hamiltonian for the rare $b \to s l^+ l^-$ transition at the hadronic scale is given by

$$\begin{aligned} \mathcal{H}_{\rm eff} = -\frac{4G_{\rm F}}{\sqrt{2}}V_{ts}^*V_{tb}\Bigg[&C_1O_1^c + C_2O_2^c + \sum_{i=3}^{6}C_iO_i \\ &+ \sum_{i=7}^{10}(C_iO_i + C_i'O_i') + \sum_{i=S,P}(C_iO_i + C_i'O_i')\Bigg], \end{aligned} \quad (12)$$

where the effective operators O_i $(i = 1,2,\ldots,10,S,P)$ and O_i' $(i = 7,8,\ldots,10,S,P)$ are expressed as [51−55]

$$\begin{aligned} O_1^c &= (\bar{s}_L\gamma_\mu T^a c_L)(\bar{c}_L\gamma^\mu T^a b_L), \\ O_2^c &= (\bar{s}_L\gamma_\mu c_L)(\bar{c}_L\gamma^\mu b_L), \\ O_3 &= (\bar{s}_L\gamma_\mu b_L)\sum_q(\bar{q}\gamma^\mu q), \\ O_4 &= (\bar{s}_L\gamma_\mu T^a b_L)\sum_q(\bar{q}\gamma^\mu T^a q), \\ O_5 &= (\bar{s}_L\gamma_\mu\gamma_\nu\gamma_\rho b_L)\sum_q(\bar{q}\gamma^\mu\gamma^\nu\gamma^\rho q), \\ O_6 &= (\bar{s}_L\gamma_\mu\gamma_\nu\gamma_\rho T^a b_L)\sum_q(\bar{q}\gamma^\mu\gamma^\nu\gamma^\rho T^a q), \\ O_7 &= \frac{e}{16\pi^2}m_b(\bar{s}_L\sigma_{\mu\nu}b_R)F^{\mu\nu}, \\ O_7' &= \frac{e}{16\pi^2}m_b(\bar{s}_R\sigma_{\mu\nu}b_L)F^{\mu\nu}, \\ O_8 &= \frac{g_{\rm s}}{16\pi^2}m_b(\bar{s}_L\sigma_{\mu\nu}T^a b_R)G^{a,\mu\nu}, \end{aligned}$$

CPC Accepted

$$
\begin{aligned}
&O'_8 = \frac{g_s}{16\pi^2} m_b (\bar{s}_R \sigma_{\mu\nu} T^a b_L) G^{a,\mu\nu},\\
&O_9 = \frac{e^2}{g_s^2} (\bar{s}_L \gamma_\mu b_L) \bar{l}\gamma^\mu l, \quad O'_9 = \frac{e^2}{g_s^2} (\bar{s}_R \gamma_\mu b_R) \bar{l}\gamma^\mu l,\\
&O_{10} = \frac{e^2}{g_s^2} (\bar{s}_L \gamma_\mu b_L) \bar{l}\gamma^\mu\gamma_5 l, \quad O'_{10} = \frac{e^2}{g_s^2} (\bar{s}_R \gamma_\mu b_R) \bar{l}\gamma^\mu\gamma_5 l,\\
&O_S = \frac{e^2}{16\pi^2} m_b (\bar{s}_L b_R) \bar{l} l, \quad O'_S = \frac{e^2}{16\pi^2} m_b (\bar{s}_R b_L) \bar{l} l,\\
&O_P = \frac{e^2}{16\pi^2} m_b (\bar{s}_L b_R) \bar{l}\gamma_5 l, \quad O'_P = \frac{e^2}{16\pi^2} m_b (\bar{s}_R b_L) \bar{l}\gamma_5 l, \qquad (13)
\end{aligned}
$$

Here, g_s denotes the strong coupling constant, $F^{\mu\nu}$ and $G^{\mu\nu}$ denote the electromagnetic and gluon field strength tensors, respectively, and T^a (with $a = 1,\ldots,8$) are the generators of the $SU(3)$ group.

Because many unknown parameters affect the quark mass eigenstates and mixing matrices, which in turn determine flavor-changing vertices, we adopt the mass insertion approximation (MIA) to evaluate the supersymmetric contributions to flavor-changing neutral current (FCNC) processes. In this framework, the fermion and sfermion states are expressed in a basis in which all couplings to neutral gaugino fields are flavor diagonal. Flavor-changing effects arise solely from the off-diagonal elements of the squark propagators, allowing the pattern of flavor violation to be systematically expressed in terms of mass insertion parameters. The relevant flavor-violating parameters are defined as follows:

$$
\tilde{M}^2_{q_{ij}} \simeq M^2_{\tilde{q}} (1 + \delta^{AB}_{ij}) \qquad (14)
$$

where $M_{\tilde{q}}$ is the common squark mass; $AB = LL, LR, RR$ denotes the chirality structure; $i, j = 1,2,3$ are the generation indices; and $q = u, d$ labels the up- and down-type squarks. Since we focus on the $b \to s$ decay process, only mixing terms involving the second and third generations are considered. The relevant flavor-violating parameters are assumed to satisfy:

$$
\delta^{AB}_{23} \equiv \delta^{U,AB}_{23} = \delta^{D,AB}_{23}, \quad AB = LL, LR, RR. \qquad (15)
$$

The flavor-violating parameters δ^{AB}_{23} originate from trilinear scalar couplings and flavor-violating scalar mass terms in the soft-breaking terms. For simplicity, we assume that the second- and third-generation flavor-changing mass insertions are identical in the up- and down-type squark sectors. The primary Feynman diagrams contributing to the process $b \to s l^+ l^-$ in the $\mu\nu$SSM are shown in Fig. 1. Here, χ_k $(k = 1,\ldots,5)$ denote charginos, χ^0_j $(j = 1,\ldots,10)$ denote neutralinos, S_l $(l = 1,\ldots,8)$ denote neutral scalars, U_i $(i = 1,\ldots,6)$ denote up-type squarks, D_i $(i = 1,\ldots,6)$ denote down-type squarks, S^-_l $(l = 2,\ldots,8)$ denote charged scalars, and $\tilde{g}$ denotes the gluino. Because of the large number of possible mass insertions, they are not explicitly marked in the diagrams; however, all insertions are included in the calculation of the Wilson coefficients. At the electroweak scale $\mu_{\rm EW}$, the relevant Wilson coefficients are separated into

$$
\begin{aligned}
C_{7,\rm NP}(\mu_{EW}) &= C_{7,S^\pm}(\mu_{EW}) + C_{7,\chi^\pm}(\mu_{EW}) + C_{7,\chi^0}(\mu_{EW})\\
&\quad + C_{7,\tilde{g}}(\mu_{EW}),\\
C_{8,\rm NP}(\mu_{EW}) &= C_{8,S^\pm}(\mu_{EW}) + C_{8,\chi^\pm}(\mu_{EW}) + C_{8,\chi^0}(\mu_{EW})\\
&\quad + C_{8,\tilde{g}}(\mu_{EW}),\\
C_{9,\rm NP}(\mu_{EW}) &= C^{\gamma}_{9,\rm NP}(\mu_{EW}) + C^{Z}_{9,\rm NP}(\mu_{EW}) + C^{box}_{9,\rm NP}(\mu_{EW}),\\
C_{10,\rm NP}(\mu_{EW}) &= C^{\gamma}_{10,\rm NP}(\mu_{EW}) + C^{Z}_{10,\rm NP}(\mu_{EW}) + C^{box}_{10,\rm NP}(\mu_{EW}),\\
C_{S,\rm NP}(\mu_{EW}) &= \sum_{l=1}^{2} C^{S_l}_{S,\rm NP}(\mu_{EW}) + C^{box}_{S,\rm NP}(\mu_{EW}),\\
C_{P,\rm NP}(\mu_{EW}) &= C^{S_l}_{P,\rm NP}(\mu_{EW}) + C^{box}_{P,\rm NP}(\mu_{EW}).
\end{aligned} \qquad (16)
$$

Here, the subscript NP denotes contributions from new physics. The symbols γ, Z, S_l, and box indicate that corrections to the corresponding Wilson coefficients arise from γ-, Z-, and S_l-penguin diagrams, as well as box diagrams. For clarity, we further decompose these contributions as follows:

$$
\begin{aligned}
C^{\gamma}_{9,\rm NP}(\mu_{EW}) &= C^{\gamma}_{9,S^\pm}(\mu_{EW}) + C^{\gamma}_{9,\chi^\pm}(\mu_{EW}) + C^{\gamma}_{9,\chi^0}(\mu_{EW})\\
&\quad + C^{\gamma}_{9,\tilde{g}}(\mu_{EW}),\\
C^{Z}_{9,\rm NP}(\mu_{EW}) &= (4s^2_W - 1) C^{Z}_{10,\rm NP}(\mu_{EW}),\\
C^{Z}_{10,\rm NP}(\mu_{EW}) &= C^{Z}_{10,S^\pm}(\mu_{EW}) + C^{Z}_{10,\chi^\pm}(\mu_{EW}) + C^{Z}_{10,\chi^0}(\mu_{EW})\\
&\quad + C^{Z}_{10,\tilde{g}}(\mu_{EW}),\\
C^{S_l}_{S,\rm NP}(\mu_{EW}) &= C^{S_l}_{S,S^\pm}(\mu_{EW}) + C^{S_l}_{S,\chi^\pm}(\mu_{EW}) + C^{S_l}_{S,\chi^0}(\mu_{EW})\\
&\quad + C^{S_l}_{S,\tilde{g}}(\mu_{EW}),\\
C^{S_l}_{P,\rm NP}(\mu_{EW}) &= C^{S_l}_{P,S^\pm}(\mu_{EW}) + C^{S_l}_{P,\chi^\pm}(\mu_{EW}) + C^{S_l}_{P,\chi^0}(\mu_{EW})\\
&\quad + C^{S_l}_{P,\tilde{g}}(\mu_{EW}),\\
C^{box}_{9,\rm NP}(\mu_{EW}) &= C^{box}_{9,S^\pm}(\mu_{EW}) + C^{box}_{9,\chi^\pm}(\mu_{EW}) + C^{box}_{9,\chi^0}(\mu_{EW})\\
&\quad + C^{box}_{9,\tilde{g}}(\mu_{EW}),\\
C^{box}_{10,\rm NP}(\mu_{EW}) &= C^{box}_{10,S^\pm}(\mu_{EW}) + C^{box}_{10,\chi^\pm}(\mu_{EW}) + C^{box}_{10,\chi^0}(\mu_{EW})\\
&\quad + C^{box}_{10,\tilde{g}}(\mu_{EW}),\\
C^{box}_{S,\rm NP}(\mu_{EW}) &= C^{box}_{S,S^\pm}(\mu_{EW}) + C^{box}_{S,\chi^\pm}(\mu_{EW}) + C^{box}_{S,\chi^0}(\mu_{EW})\\
&\quad + C^{box}_{S,\tilde{g}}(\mu_{EW}),\\
C^{box}_{P,\rm NP}(\mu_{EW}) &= C^{box}_{P,S^\pm}(\mu_{EW}) + C^{box}_{P,\chi^\pm}(\mu_{EW}) + C^{box}_{P,\chi^0}(\mu_{EW})\\
&\quad + C^{box}_{P,\tilde{g}}(\mu_{EW}).
\end{aligned} \qquad (17)
$$

CPC Accepted

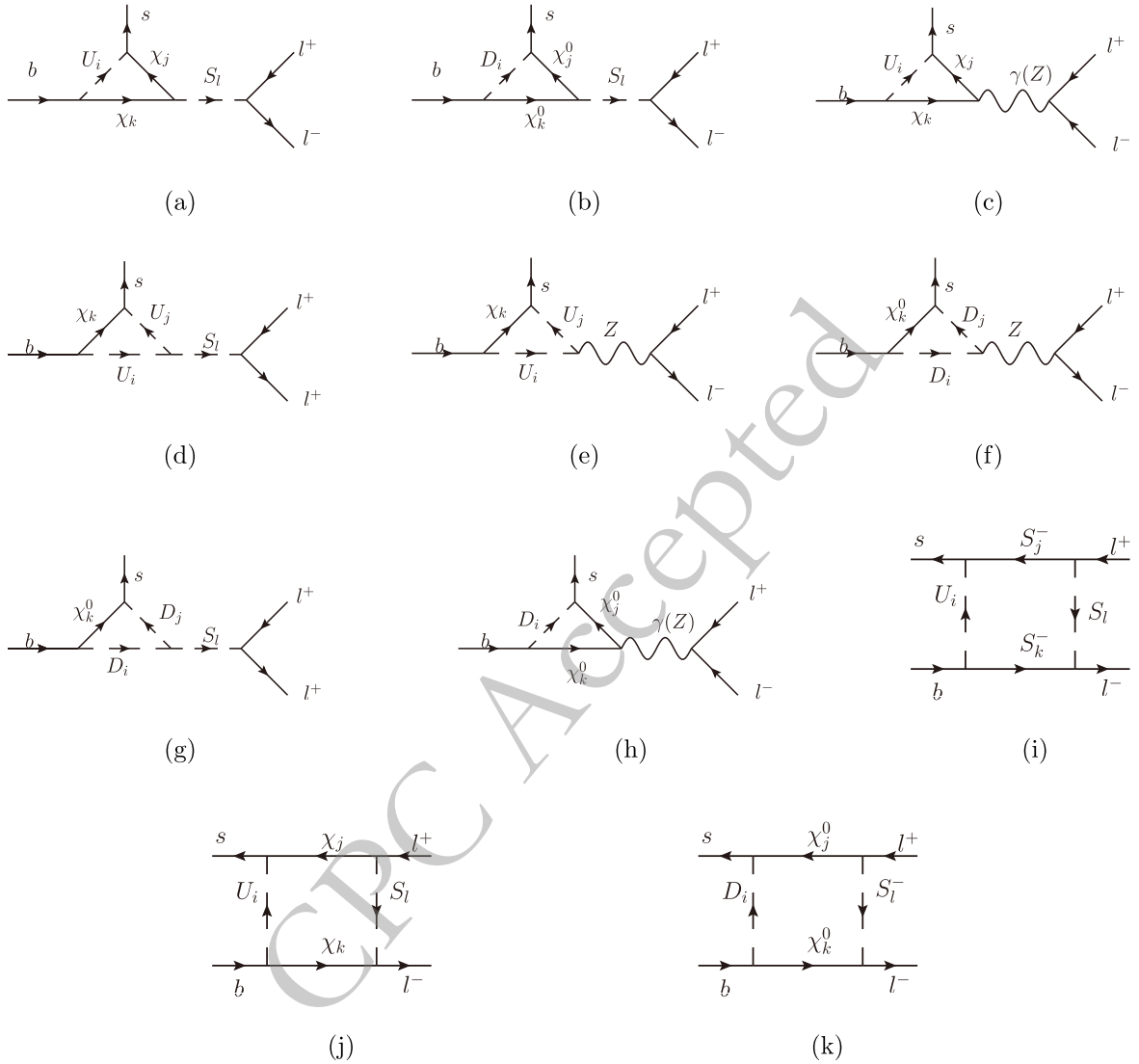

CPC Accepted

Fig. 1. Feynman diagrams that contribute to the $b \to s l^+ l^-$ transition in the $\mu\nu$SSM.

The detailed expressions for these Wilson coefficients are provided in the Supplemental Material. These Wilson coefficients form the basis for our calculations, and the dominant contributions are identified in the subsequent numerical analysis. According to Eq. (27), the coefficients C_7 and C_9 are always correlated with the other C_i through definite linear combinations. It is therefore convenient to define the effective coefficients $C_7^{\rm eff}$, $C_9^{\rm eff}$, as well as $C_8^{\rm eff}$ and $C_{10}^{\rm eff}$, which are given by [56]

$$\begin{aligned}
C_7^{\rm eff} &= \frac{4\pi}{\alpha_s}C_7 - \frac{1}{3}C_3 - \frac{4}{9}C_4 - \frac{20}{3}C_5 - \frac{80}{9}C_6,\\
C_8^{\rm eff} &= \frac{4\pi}{\alpha_s}C_8 + C_3 - \frac{1}{6}C_4 + 20C_5 - \frac{10}{3}C_6,\\
C_9^{\rm eff} &= C_9^{\rm eff,SM} + Y(q^2),\\
C_{10}^{\rm eff} &= \frac{4\pi}{\alpha_s}C_{10}, \quad C'^{\rm eff}_{7,8,9,10} = \frac{4\pi}{\alpha_s}C'_{7,8,9,10},
\end{aligned} \tag{18}$$

where the functions $Y(q^2)$ are given by

$$\begin{aligned}
\mathrm{Y}(q^2) = {} & \mathrm{h}(q^2, m_c)\Big(\frac{4}{3}C_1 + C_2 + 6C_3 + 60C_5\Big)\\
& - \frac{1}{2}\mathrm{h}(q^2, m_b)\Big(7C_3 + \frac{4}{3}C_4 + 76C_5 + \frac{64}{3}C_6\Big)\\
& - \frac{1}{2}\mathrm{h}(q^2, 0)\Big(C_3 + \frac{4}{3}C_4 + 16C_5 + \frac{64}{3}C_6\Big)\\
& + \frac{4}{3}C_3 + \frac{64}{9}C_5 + \frac{64}{27}C_6.
\end{aligned} \tag{19}$$

The function

$$\mathrm{h}(q^2, m_q) = -\frac{4}{9}\Big(\ln\frac{m_q^2}{\mu^2} - \frac{2}{3} - z\Big)$$

$$-\frac{4}{9}(2+z)\sqrt{|z-1|}\begin{cases}\arctan\dfrac{1}{\sqrt{z-1}}, & z>1,\\ \ln\dfrac{1+\sqrt{1-z}}{\sqrt{z}}-\dfrac{\mathrm{i}\pi}{2}, & z\le 1,\end{cases} \tag{20}$$

with $z=4m_q^2/q^2$. The Wilson coefficients at the hadronic scale are computed in the SM at next-to-next-to-leading-logarithmic (NNLL) accuracy and are listed in Table 1 [57]. In addition, the Wilson coefficients in Eq. (16) are evaluated at the matching scale $\mu_{\rm EW}$ and evolved down to the hadronic scale $\mu\sim m_b$ by solving the renormalization group equations.

$$\vec{C}_{\rm NP}(\mu)=\widehat{U}(\mu,\mu_0)\vec{C}_{\rm NP}(\mu_0), \tag{21}$$

$$\vec{C}'_{\rm NP}(\mu)=\widehat{U}'(\mu,\mu_0)\vec{C}'_{\rm NP}(\mu_0). \tag{22}$$

with

Table 1. The effective SM Wilson coefficients are evaluated at the hadronic scale $\mu=m_b\simeq 4.8$ GeV at NNLL accuracy.

$C_7^{\rm eff,SM}$	$C_8^{\rm eff,SM}$	$C_9^{\rm eff,SM}$	$C_{10}^{\rm eff,SM}$
−0.304	−0.167	4.211	−4.103

$$\begin{aligned}\vec{C}_{\rm NP}^{\,T}&=\left(C_{1,\rm NP},\cdots,C_{6,\rm NP},C_{7,\rm NP}^{eff},C_{8,\rm NP}^{eff},C_{9,\rm NP}^{eff}-Y(q^2),C_{10,\rm NP}^{eff}\right)\\ \vec{C}_{\rm NP}^{\prime T}&=\left(C_{7,\rm NP}^{\prime eff},C_{8,\rm NP}^{\prime eff},C_{9,\rm NP}^{\prime eff},C_{10,\rm NP}^{\prime eff}\right).\end{aligned} \tag{23}$$

Accordingly, the evolving matrices are treated as

$$\begin{aligned}\widehat{U}(\mu,\mu_0)&\simeq 1-\left[\frac{1}{2\beta_0}\ln\frac{\alpha_s(\mu)}{\alpha_s(\mu_0)}\right]\widehat{\gamma}^{\rm eff(0),\,T},\\ \widehat{U'}(\mu,\mu_0)&\simeq 1-\left[\frac{1}{2\beta_0}\ln\frac{\alpha_s(\mu)}{\alpha_s(\mu_0)}\right]\widehat{\gamma'}^{\rm eff(0),\,T},\end{aligned} \tag{24}$$

where the anomalous-dimension matrices are computed in Ref. [58]

$$\widehat{\gamma}^{\rm eff(0)}=\begin{pmatrix}
-4 & \frac{8}{3} & 0 & -\frac{2}{9} & 0 & 0 & -\frac{208}{243} & \frac{173}{162} & -\frac{2272}{729} & 0\\
12 & 0 & 0 & \frac{4}{3} & 0 & 0 & \frac{416}{81} & \frac{70}{27} & \frac{1952}{243} & 0\\
0 & 0 & 0 & -\frac{52}{3} & 0 & 2 & -\frac{176}{81} & \frac{14}{27} & -\frac{6752}{243} & 0\\
0 & 0 & -\frac{40}{9} & -\frac{100}{9} & \frac{4}{9} & \frac{5}{6} & -\frac{152}{243} & -\frac{587}{162} & -\frac{2192}{729} & 0\\
0 & 0 & 0 & -\frac{256}{3} & 0 & 20 & -\frac{6272}{81} & \frac{6596}{27} & -\frac{84032}{243} & 0\\
0 & 0 & -\frac{256}{9} & \frac{56}{9} & \frac{40}{9} & -\frac{2}{3} & \frac{4624}{243} & \frac{4772}{81} & -\frac{37856}{729} & 0\\
0 & 0 & 0 & 0 & 0 & 0 & \frac{32}{3} & 0 & 0 & 0\\
0 & 0 & 0 & 0 & 0 & 0 & -\frac{32}{9} & \frac{28}{3} & 0 & 0\\
0 & 0 & 0 & 0 & 0 & 0 & 0 & 0 & 0 & 0\\
0 & 0 & 0 & 0 & 0 & 0 & 0 & 0 & 0 & 0
\end{pmatrix}, \tag{25}$$

$$\widehat{\gamma'}^{\rm eff(0)}=\begin{pmatrix}
\frac{32}{3} & 0 & 0 & 0\\
-\frac{32}{9} & \frac{28}{3} & 0 & 0\\
0 & 0 & 0 & 0\\
0 & 0 & 0 & 0
\end{pmatrix}. \tag{26}$$

CPC Accepted

IV. DECAY BRANCHING RATIOS AND FORWARD-BACKWARD ASYMMETRIES

Using the effective Hamiltonian above and neglecting the s-quark mass, the matrix element for the quark-level transition $b \to s l^+ l^-$ is [59]

$$\begin{aligned}\mathcal{M} = \frac{\alpha G_F}{\sqrt{2}\pi} V_{tb}V_{ts}^* \Big\{ &\left[C_9^{\rm eff}\bar{s}_L\gamma_\mu b_R + C_9'^{\rm eff}\bar{s}_R\gamma_\mu b_R\right](\bar{l}\gamma^\mu l) + \left[C_{10}^{\rm eff}\bar{s}_L\gamma_\mu b_R + C_{10}'^{\rm eff}\bar{s}_R\gamma_\mu b_L\right](\bar{l}\gamma^\mu\gamma^5 l)\\ &+ 2i\frac{q^\nu}{q^2}\left[\sigma_{\mu\nu}\left(C_7^{\rm eff}\bar{s}_L m_b b_R + C_7'^{\rm eff}\bar{s}_R m_b b_L\right)\right](\bar{l}\gamma^\mu l) + \left[C_S\bar{s}_L b_R + C_S'\bar{s}_R b_L\right](\bar{l}l) + \left[C_P\bar{s}_L b_R + C_P'\bar{s}_R b_L\right](\bar{l}\gamma_5 l)\Big\}. \end{aligned} \tag{27}$$

Using the matrix element in Eq. (27), the differential decay rate is derived as

$$\begin{aligned}\frac{d^2\Gamma}{dq^2 d\cos\theta} = &\frac{\alpha_{\rm EW}^2}{16\pi^2}\frac{G_F^2 m_b^5 |V_{tb}V_{ts}^*|^2}{48\pi^3}\left(1-\frac{q^2}{m_b^2}\right)^2\left(1-\frac{4m_l^2}{q^2}\right)^{1/2}\times\Big\{12\left(1+\frac{2m_l^2}{q^2}\right)\Re\left(C_7^{\rm eff}C_9^{\rm eff*}(q^2)\right)+\frac{6m_l^2}{m_b^2}\left[|C_9^{\rm eff}(q^2)|^2-|C_{10}^{\rm eff}|^2\right]\\ &+6|C_7^{\rm eff}|^2\left[1+\frac{m_b^2}{q^2}-\left(1-\frac{m_b^2}{q^2}-\frac{4m_l^2}{q^2}+\frac{4m_l^2m_b^2}{q^4}\right)\cos^2\theta+\frac{4m_l^2m_b^2}{q^4}\right]\\ &+\frac{3}{2}\left[|C_9^{\rm eff}(q^2)|^2+|C_{10}^{\rm eff}|^2\right]\left[1+\frac{q^2}{m_b^2}-\left(1-\frac{q^2}{m_b^2}-\frac{4m_l^2}{q^2}+\frac{4m_l^2}{m_b^2}\right)\cos^2\theta\right]\\ &-\frac{6m_l^2}{m_b^2}|C_S|^2+\frac{3q^2}{2m_b^2}\left(|C_S|^2+|C_P|^2\right)+\left[\frac{6q^2}{m_b^2}\Re\left(C_9^{\rm eff}(q^2)C_{10}^{\rm eff*}\right)+12\Re\left(C_7^{\rm eff}C_{10}^{\rm eff*}\right)\right]\sqrt{1-\frac{4m_l^2}{q^2}}\cos\theta\\ &+\frac{6m_l}{m_b}\left[\Re\left(C_9^{\rm eff}(q^2)C_S^*+2C_7^{\rm eff}C_S^*\right)\sqrt{1-\frac{4m_l^2}{q^2}}\cos\theta+\Re\left(C_{10}C_P^*\right)\right]\Big\}. \end{aligned} \tag{28}$$

The normalized differential branching ratio for $B \to X_s l^+ l^-$ is given by

$$\begin{aligned}R(q^2) = \frac{d{\rm Br}(B\to X_s l^+ l^-)}{\Gamma(B\to X_c e\nu)dq^2} = &\frac{\alpha_{\rm EW}^2}{2\pi^2}\frac{|V_{tb}V_{ts}^*|^2}{|V_{cb}|^2}\frac{1}{f(z)\kappa(z)}\left(1-\frac{q^2}{m_b^2}\right)^2\sqrt{1-\frac{4m_l^2}{q^2}}\times\Big\{12\left(1+\frac{2m_l^2}{q^2}\right)\Re(C_7^{\rm eff}C_9^{\rm eff*}(q^2))\\ &+4|C_7^{\rm eff}|^2\left[1+2\frac{m_b^2}{q^2}+\frac{2m_l^2}{q^2}+\frac{4m_l^2m_b^2}{q^4}\right]+|C_9^{\rm eff}(q^2)|^2\left[1+2\frac{q^2}{m_b^2}+\frac{2m_l^2}{q^2}+\frac{4m_l^2}{m_b^2}\right]\\ &+|C_{10}^{\rm eff}|^2\left[1+2\frac{q^2}{m_b^2}+\frac{2m_l^2}{q^2}-\frac{8m_l^2}{m_b^2}\right]-\frac{6m_l^2}{m_b^2}|C_S|^2+\frac{3q^2}{2m_b^2}\left(|C_S|^2+|C_P|^2\right)+\frac{6m_l}{m_b}\Re(C_{10}^{\rm eff}C_P^*)\Big\}. \end{aligned} \tag{29}$$

The normalized differential branching ratio is defined in terms of the semileptonic decay width of the B meson, thereby reducing uncertainties associated with the bottom-quark mass and CKM matrix elements. The corresponding formula is given by [16]

$$\Gamma(B\to X_c e\bar{\nu}_e) = \frac{G_F^2 m_b^5}{192\pi^3}|V_{cb}|^2 f(z)\kappa(z). \tag{30}$$

Here, $f(z) = 1-8z^2+8z^6-z^8-24z^4\ln z$ and $\kappa(z) = 1-\frac{2\alpha_s}{3\pi}\left[(\pi^2-\frac{31}{4})(1-z)^2+\frac{3}{2}\right]$ are the phase-space factor and QCD correction factor, respectively ($z = m_c/m_b$) [52]. The unnormalized forward–backward asymmetry is given by

$$\bar{A}_{FB}(q^2) = \frac{1}{\Gamma(B\to X_c e\nu)}\int_{-1}^{1} d\cos\theta\frac{d^2\Gamma(B\to X_s l^+ l^-)}{d\cos\theta dq^2}{\rm sgn}(\cos\theta)$$

$$\begin{aligned}= &\frac{3\alpha_{\rm EW}^2}{2\pi^2}\left|\frac{V_{tb}V_{ts}^*}{V_{cb}}\right|^2\frac{1}{f(z)\kappa(z)}\left(1-\frac{q^2}{m_b^2}\right)^2\left(1-\frac{4m_l^2}{q^2}\right)\\ &\times\left\{\frac{q^2}{m_b^2}\Re\left(C_9^{\rm eff}(q^2)C_{10}^{\rm eff*}\right)+2\Re\left(C_7^{\rm eff}C_{10}^{\rm eff*}\right)\right.\\ &\left.+\frac{m_l}{m_b}\Re\left(C_9^{\rm eff}(q^2)C_S^*+2C_7^{\rm eff}C_S^*\right)\right\}, \end{aligned} \tag{31}$$

and the normalized forward–backward asymmetry is given by

$$A_{FB}(q^2) = \frac{1}{R(q^2)}\bar{A}_{FB}(q^2). \tag{32}$$

The global forward–backward asymmetry over the region $q^2 \in [a, b]$ GeV^2 is given by [60]

CPC Accepted

$$\frac{N(\ell_+^+)-N(\ell_+^-)}{N(\ell_+^+)+N(\ell_+^-)} \equiv \frac{\int_{-1}^{1}\mathrm{d}(\cos\theta)\int \mathrm{d}s\,\dfrac{\mathrm{d}^2\Gamma(B\to X_s\ell^+\ell^-)}{\mathrm{d}(\cos\theta)\,\mathrm{d}s}\mathrm{sgn}(\cos\theta)}{\int_{-1}^{1}\mathrm{d}(\cos\theta)\int \mathrm{d}s\,\dfrac{\mathrm{d}^2\Gamma(B\to X_s\ell^+\ell^-)}{\mathrm{d}(\cos\theta)\,\mathrm{d}s}}. \tag{33}$$

The SM predictions for $\mathrm{BR}(B\to X_s e^+e^-)$ and $\mathrm{BR}(B\to X_s\mu^+\mu^-)$ in the low-q^2 region, including nonperturbative effects evaluated using an updated Krüger–Sehgal (KS) analysis, are [14]

$$\begin{aligned}&\mathrm{BR}(B\to X_s e^+e^-)^{\mathrm{SM}}_{q^2\in[1,6]\,\mathrm{GeV}^2}=(1.78\pm0.13)\times10^{-6},\\&\mathrm{BR}(B\to X_s\mu^+\mu^-)^{\mathrm{SM}}_{q^2\in[1,6]\,\mathrm{GeV}^2}=(1.73\pm0.13)\times10^{-6}.\end{aligned} \tag{34}$$

The SM predictions for the branching ratios $\mathrm{BR}(B\to X_s e^+e^-)$ and $\mathrm{BR}(B\to X_s\mu^+\mu^-)$ in the high-q^2 region are given by [14]

$$\begin{aligned}&\mathrm{BR}(B\to X_s e^+e^-)^{\mathrm{SM}}_{q^2\in[14.4,25]\,\mathrm{GeV}^2}=(2.04\pm0.87)\times10^{-7},\\&\mathrm{BR}(B\to X_s\mu^+\mu^-)^{\mathrm{SM}}_{q^2\in[14.4,25]\,\mathrm{GeV}^2}=(2.38\pm0.87)\times10^{-7}.\end{aligned} \tag{35}$$

In our analysis, the lepton-flavor-averaged branching ratio for $B\to X_s l^+l^-$ is obtained by averaging the branching ratios for the electron and muon final states.

V. NUMERICAL ANALYSIS

In this section, we present a systematic numerical analysis of the inclusive decay $B\to X_s l^+l^-$ within the $\mu\nu$SSM, focusing on the new-physics contributions to the relevant Wilson coefficients and their underlying mechanisms. We first examine the parameter dependence of $C_{9,\mathrm{NP}}$ and $C_{10,\mathrm{NP}}$, as well as the relative sizes of the dominant loop effects arising from the extended fermion and scalar sectors of the $\mu\nu$SSM. We then investigate how these corrections affect the interference among the relevant Wilson coefficients and, consequently, the branching ratios and forward-backward asymmetries in the low- and high-q^2 regions. To obtain clear numerical results, we adopt specific assumptions [61] for selected parameters in the $\mu\nu$SSM. These assumptions are as follows:

$$\begin{aligned}&\kappa_{ijk}=\kappa\delta_{ij}\delta_{jk},\quad (A_\kappa\kappa)_{ijk}=A_\kappa\kappa\delta_{ij}\delta_{jk},\quad \lambda_i=\lambda,\\&(A_\lambda\lambda)_i=A_\lambda\lambda,\quad Y_{e_{ij}}=Y_{e_i}\delta_{ij},\quad (A_eY_e)_{ij}=A_eY_{e_i}\delta_{ij},\\&Y_{\nu_{ij}}=Y_{\nu_i}\delta_{ij},\quad (A_\nu Y_\nu)_{ij}=a_{\nu_i}\delta_{ij},\quad m^2_{\tilde\nu^c_{ij}}=m^2_{\tilde\nu^c_i}\delta_{ij},\\&m^2_{\tilde L_{ij}}=m^2_{\tilde L}\delta_{ij},\quad m^2_{\tilde e^c_{ij}}=m^2_{\tilde e^c}\delta_{ij},\quad \upsilon_{\nu^c_i}=\upsilon_{\nu^c}.\end{aligned} \tag{36}$$

where $i,j,k=1,2,3$. Using constraints from the quark and lepton masses, we can define the following expressions:

$$Y^i_e=\frac{m^i_l}{\upsilon_d},\quad Y^i_u=\frac{m^i_u}{\upsilon_u},\quad Y^i_d=\frac{m^i_d}{\upsilon_d}. \tag{37}$$

where m^i_l, m^i_u and m^i_d represent the charged-lepton, up-quark, and down-quark masses, respectively. The corresponding numerical values can be obtained from the PDG [62]. In addition, the soft masses $m^2_{H_d}$, $m^2_{H_u}$, $m^2_{\tilde\nu^c_{ij}}$, and $m^2_{\tilde L_{ij}}$ can be calculated from the minimization conditions of the tree-level neutral scalar potential; their explicit forms are given in Ref. [42].

As discussed in our earlier work [45], the Yukawa coupling $Y_{\nu_i}\sim O(10^{-7})$ and the left-handed sneutrino VEVs $\upsilon_{\nu_i}\sim O(10^{-4}\,\mathrm{GeV})$ are governed by the TeV-scale seesaw mechanism. The resulting new-physics corrections to the $B\to X_s l^+l^-$ observables are of order $O(10^{-5})$, which is much smaller than the typical experimental and theoretical uncertainties. These effects are therefore neglected throughout our numerical analysis, and we set $Y_{\nu_i}=0$ and $\upsilon_{\nu_i}=0$.

Based on the analysis of the $\mu\nu$SSM parameter space in Ref. [42], and for simplicity, we choose the benchmark parameter values $\lambda=0.135$, $A_\kappa=-300\,\mathrm{GeV}$, $m_{\tilde L_{1,2,3}}=m_{\tilde e^c_{1,2,3}}=700\,\mathrm{GeV}$ and $A_{u_{1,2}}=A_{d_{1,2,3}}=A_{e_{1,2,3}}=1\,\mathrm{TeV}$. Given the strong constraints from direct searches at the LHC [63, 64], we take $m_{\tilde Q_{1,2,3}}=m_{\tilde u^c_{1,2}}=m_{\tilde d^c_{1,2,3}}=3\,\mathrm{TeV}$. Using the approximate GUT relation, we set the gaugino Majorana masses as $M_1=0.5M_2$ and $M_3=2.7M_2$. For certain R-parity-violating simplified SUSY scenarios, the gluino mass $m_{\tilde g}\approx M_3$ is subject to a lower bound of 2.4 TeV [62, 65]. In light of this constraint, we choose $M_2=1\,\mathrm{TeV}$, which yields $m_{\tilde g}\approx M_3=2.7\,\mathrm{TeV}$. Because A_t and $m_{\tilde u^c_3}$ significantly affect the SM Higgs mass, we choose $A_t=2.6\,\mathrm{TeV}$ and $m_{\tilde u^c_3}=3\,\mathrm{TeV}$ to obtain $m_h\approx125\,\mathrm{GeV}$. The relevant SM input parameters are summarized in Table 2.

Moreover, the measured average branching ratios for $B^0_s\to\mu^+\mu^-$ and $\bar B\to X_s\gamma$ are expressed as [62, 66–70]

$$\begin{aligned}&\mathrm{BR}(B^0_s\to\mu^+\mu^-)=(3.34\pm0.27)\times10^{-9},\\&\mathrm{BR}(\bar B\to X_s\gamma)=(3.49\pm0.19)\times10^{-4}.\end{aligned} \tag{38}$$

In the SM, the predicted branching ratios for $B^0_s\to\mu^+\mu^-$ and $\bar B\to X_s\gamma$ are [71–74]

$$\begin{aligned}&\mathrm{BR}(B^0_s\to\mu^+\mu^-)=(3.64\pm0.12)\times10^{-9},\\&\mathrm{BR}(\bar B\to X_s\gamma)=(3.40\pm0.17)\times10^{-4}.\end{aligned} \tag{39}$$

To avoid tachyons in the sneutrino sector, the sneutrino mass spectrum must be analyzed. Specifically, the left-handed sneutrino masses are predominantly determined by the soft SUSY-breaking mass $m_{\tilde L}$, whereas the three right-handed sneutrinos remain essentially degener-

CPC Accepted

Table 2. SM input parameters [62] used in the numerical analysis.

Parameter	Value
$m_B = 5279.63 \pm 0.20\,\text{MeV}$	$m_{K^*} = 0.896\,\text{GeV}$
$m_{B_s^0} = 5366.93 \pm 0.10\,\text{MeV}$	$m_\mu = 105.6583755 \pm 0.0000023\,\text{MeV}$
$m_W = 80.3692 \pm 0.0133\,\text{GeV}$	$m_Z = 91.1880 \pm 0.0020\,\text{GeV}$
$\tau_B = (1.519 \pm 0.004)\,\text{ps}$ [66]	$\alpha_s(m_Z) = 0.1180(9)$
$\tau_{B_s^0} = (1.527 \pm 0.011)\,\text{ps}$ [66]	$\alpha_{\text{em}}(m_Z) = 1/127.944(14)$
$m_c(m_c) = 1.2730 \pm 0.0046\,\text{GeV}$	$m_b(m_b) = 4.183 \pm 0.007\,\text{GeV}$
$m_t^{\text{pole}} = 172.4 \pm 0.7\,\text{GeV}$	$\lvert V_{ts}\rvert = (41.5 \pm 0.9) \times 10^{-3}$
$\lvert V_{tb}\rvert = 1.002 \pm 0.024$	

ate. The squared masses of the CP-even and CP-odd right-handed sneutrinos can be approximated as [50]:

$$m^2_{S_{5+i}} \approx (A_\kappa + 4\kappa\upsilon_{\nu^c})\kappa\upsilon_{\nu^c} + A_\lambda\lambda\upsilon_d\upsilon_u/\upsilon_{\nu^c} - 2\lambda^2(\upsilon_d^2 + \upsilon_u^2), \tag{40}$$

$$m^2_{P_{5+i}} \approx -3A_\kappa\kappa\upsilon_{\nu^c} + (A_\lambda/\upsilon_{\nu^c} + 4\kappa)\lambda\upsilon_d\upsilon_u - 2\lambda^2(\upsilon_d^2 + \upsilon_u^2). \tag{41}$$

Eqs. (40) and (41) show that, for large κ and in the limit $\upsilon_{\nu^c} \gg \upsilon_{u,d}$, the dominant contribution to the squared masses of the right-handed sneutrinos arises from the first term. Therefore, we can adopt the approximate relation

$$-4\kappa\upsilon_{\nu^c} \lesssim A_\kappa \lesssim 0, \tag{42}$$

to prevent the emergence of tachyonic states. Although A_κ has a minimal effect on the numerical results, the subsequent analysis shows that the parameters κ and υ_{ν^c} have noticeable effects on the branching ratios and forward-backward asymmetries.

In the $\mu\nu$SSM, in the limit $\upsilon_{\nu^c} \gg \upsilon_{u,d}$, the squared charged Higgs mass, $M^2_{H^\pm}$, can be written as

$$M^2_{H^\pm} \simeq M_A^2 + \left(1 - \frac{6s_W^2\lambda^2}{e^2}\right)m_W^2, \tag{43}$$

where the squared mass of the neutral pseudoscalar is given by

$$M_A^2 \simeq \frac{6\lambda\upsilon_{\nu^c}(A_\lambda + \kappa\upsilon_{\nu^c})}{\sin 2\beta}. \tag{44}$$

Unless otherwise stated, all numerical predictions presented in this work are obtained using the central values of the SM input parameters listed in Table 2. Uncertainties associated with the SM inputs, including quark masses and CKM matrix elements, as well as renormalization-scale variations, are not explicitly evaluated in our calculations because their effects are expected to be subleading compared with the variations induced by the SUSY parameter scans. The SUSY parameters are varied within phenomenologically allowed ranges to illustrate the dependence of the observables on these parameters, rather than to represent statistical uncertainties. Accordingly, no uncertainty bands or error bars are shown in the numerical plots and tables.

To validate the numerical framework, all new-physics contributions are systematically switched off to recover the Standard Model (SM) limit. Using the SM Wilson coefficients given in Table 1, together with the SM input parameters in Table 2, we evaluate the branching ratios $\text{BR}(B \to X_s l^+ l^-)$ and the forward-backward asymmetry $A_{\text{FB}}(B \to X_s l^+ l^-)$ for the $b \to s\ell^+\ell^-$ transition in the low- and high-q^2 regions. The branching ratios $\text{BR}(B \to X_s l^+ l^-)$ are computed using the standard approximate parametrization of [75]. The corresponding numerical results are summarized in Table 3. The resulting predictions are consistent with the SM results discussed in the Introduction within their quoted 1σ uncertainty ranges, thereby providing a check of the numerical framework used in this work.

Before presenting the numerical results, we briefly discuss the experimental constraints relevant to our parameter scan. Measurements of $B \to X_s l^+ l^-$, $\bar{B} \to X_s\gamma$, and $B_s^0 \to \mu^+\mu^-$ impose stringent constraints on the parameter space. In particular, $B_s^0 \to \mu^+\mu^-$ is sensitive to scalar and pseudoscalar contributions; therefore, through its dependence on the corresponding Wilson coefficients, this decay constrains the flavor-violating mass insertion δ_{23}^{AB}. To identify viable parameter combinations, we perform a systematic scan, treating $\tan\beta$ and κ as auxiliary parameters. Fig. 2 shows $\text{BR}(B_s^0 \to \mu^+\mu^-)$ as a function of δ_{23}^{AB}, together with the experimental 2σ bounds. In Fig. 2(a), we fix $\kappa = 0.4$, $A_\lambda = 0.6\,\text{TeV}$, and $\upsilon_{\nu^c} = 2\,\text{TeV}$, and present results for $\tan\beta = 20$ (solid line) and $\tan\beta = 30$ (dashed line). Fig. 2(b) corresponds to $\tan\beta = 25$, $A_\lambda = 0.5\,\text{TeV}$, and $\upsilon_{\nu^c} = 2\,\text{TeV}$, with curves for $\kappa = 0.06$ (solid line) and $\kappa = 0.3$ (dashed line). For the subsequent $B \to X_s l^+ l^-$ analysis, we select viable benchmark values of δ_{23}^{AB} separ-

Table 3. SM predictions for observables in $B \to X_s l^+ l^-$ decays.

Observable	Our SM prediction
$\text{BR}(B \to X_s l^+ l^-)_{q^2 \in [1,6]\,\text{GeV}^2}$	1.6×10^{-6}
$\text{BR}(B \to X_s l^+ l^-)_{q^2 \in [14.4,25]\,\text{GeV}^2}$	3.0×10^{-7}
$A_{\text{FB}}(B \to X_s l^+ l^-)_{q^2 \in [1,6]\,\text{GeV}^2}$	–0.097
$A_{\text{FB}}(B \to X_s l^+ l^-)_{q^2 \in [14.4,25]\,\text{GeV}^2}$	0.377

CPC Accepted

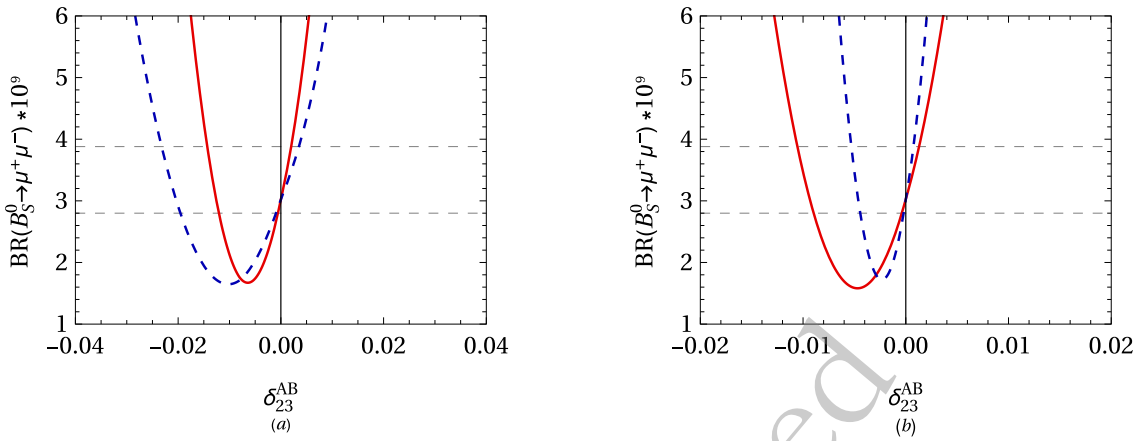

Fig. 2. (color online) Branching ratio BR($B_s^0 \to \mu^+\mu^-$) as a function of the mass-insertion parameters δ_{23}^{AB}, for (a) tanβ = 20 (solid line) and tanβ = 30 (dashed line), and (b) κ = 0.06 (solid line) and κ = 0.3 (dashed line).

ately for the tanβ and κ scans, using different fixed SUSY parameter settings. Specifically, we adopt $\delta_{23}^{AB} = 0.6\times10^{-3}$ for the tanβ scan and consider the range $(0.6-1.4)\times10^{-3}$, over which the predicted BR($B_s^0 \to \mu^+\mu^-$) varies from approximately 3.3×10^{-9} to 3.7×10^{-9}. For the κ scan, we choose $\delta_{23}^{AB} = 0.20\times10^{-3}$ and consider the range $(0.14-0.22)\times10^{-3}$, over which the predicted BR($B_s^0 \to \mu^+\mu^-$) varies from approximately 3.10×10^{-9} to 3.15×10^{-9}. Both sets of parameter choices satisfy the experimental 2σ bounds on BR($B_s^0 \to \mu^+\mu^-$). By fixing the corresponding viable values of δ_{23}^{AB} in each scan, we can examine the effects of tanβ and κ separately.

The parameter tanβ is primarily constrained by the $\bar{B} \to X_s\gamma$ decay, which is governed by the dipole Wilson coefficient C_7. The charged-Higgs contribution to C_7 exhibits the characteristic parametric dependence

$$C_7^{H^\pm} \propto x_t\left[\cot^2\beta F_1(x_t, x_{H^\pm}) - F_2(x_t, x_{H^\pm})\right], \qquad (45)$$

where $x_t = m_t^2/m_W^2$ and $x_{H^\pm} = m_{H^\pm}^2/m_W^2$.

Fig. 3 shows the allowed region of tanβ at the 2σ confidence level, subject to the SM-like Higgs mass constraint (124–126)GeV. In this region, the $B \to X_s l^+l^-$ observables remain within their respective 3σ experimental ranges and therefore impose no additional constraints. Specifically, κ is scanned from 0.01 to 0.6. The Higgs mass requirement restricts the phenomenologically viable range of κ to 0.4–0.6, and no other observables further constrain this interval. Values of κ outside this viable range are shown only to illustrate the parameter dependence of the observables.

To analyze the underlying physics of the $B \to X_s l^+l^-$ decay, we calculate the relevant Feynman diagrams (representative diagrams are shown in Fig. 1) and determine the corresponding new-physics contributions to the Wilson coefficients. The resulting theoretical predictions are then compared with experimental measurements of BR($B \to X_s l^+l^-$) and $A_{FB}(B \to X_s l^+l^-)$, allowing us to identify the Wilson coefficients that have the most significant impact on these observables.

The decay amplitude of $B \to X_s l^+l^-$ is governed primarily by the Wilson coefficients C_7, C_9, and C_{10}. To clarify the origin of the semileptonic contributions in the $\mu\nu$SSM, we investigate the tanβ dependence of $C_{9,\mathrm{NP}}$ and $C_{10,\mathrm{NP}}$ in Fig. 4.

In panel (a), we compare the full value of $C_{9,\mathrm{NP}}$ in the $\mu\nu$SSM (solid line), the chargino-mediated photon-penguin contribution $C_{9,\chi^\pm}^{\gamma}$ (dashed line), and the corresponding MSSM prediction (dash-dotted line). The close agreement between the full result and the chargino-mediated contribution indicates that the tanβ dependence of $C_{9,\mathrm{NP}}$ is primarily governed by the chargino sector. The dominant chargino-mediated contribution can be expressed schematically as

$$C_{9,\chi^\pm}^{\gamma} \propto \sum_{I,\beta}\left(-\frac{e}{s_W}Z_+^{I\beta *}R_u^{2I} + Y_c Z_+^{2\beta *}R_u^{5I}\right)Y_b Z_-^{2\beta}R_u^{3I}F_9^{I\beta}, \qquad (46)$$

where $F_9^{I\beta}$ denotes the corresponding loop-function combination incorporating the relevant mass-insertion structures. The complete expressions for the Wilson coefficients, including all mass-insertion contributions, are provided in the Supplemental Material. This expression shows that the tanβ dependence originates mainly from the bottom-quark Yukawa coupling Y_b and from the tanβ-dependent chargino mixing matrices entering the interaction vertices. The resulting variations in the vertex couplings, together with the associated mass dependence of the loop functions, modify the chargino-mediated photon-penguin amplitude and consequently affect $C_{9,\mathrm{NP}}$.

Compared with the MSSM, the distinct charged-fermion mixing structure in the $\mu\nu$SSM modifies the masses and couplings of the charged-fermion mass eigenstates entering the loop contributions, leading to a different

CPC Accepted

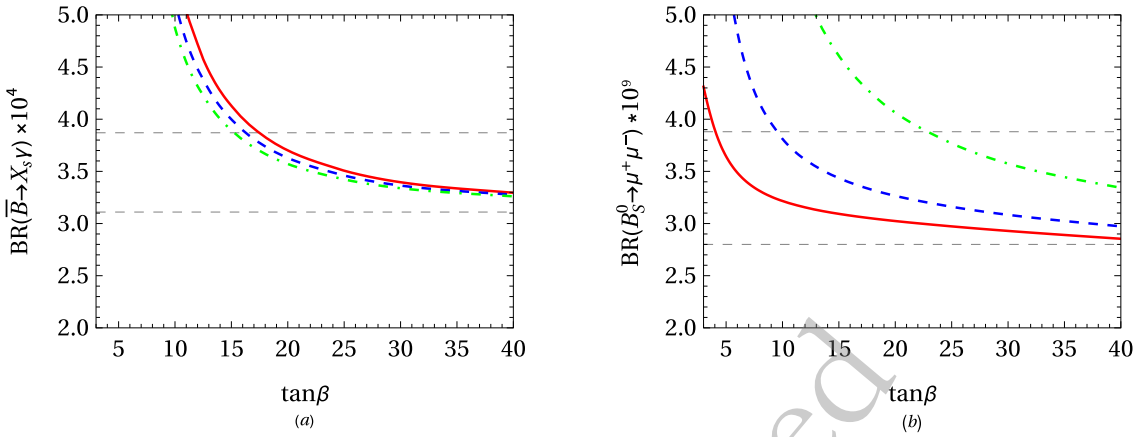

Fig. 3. (color online) For fixed $\kappa = 0.4$ and $A_\lambda = 0.6$ TeV, (a) BR($\bar{B} \to X_s\gamma$) and (b) BR($B_s^0 \to \mu^+\mu^-$) vary with tanβ for $v_{\nu^c} = 1.8$ TeV (solid line), $v_{\nu^c} = 2.0$ TeV (dashed line), and $v_{\nu^c} = 2.2$ TeV (dash-dotted line).

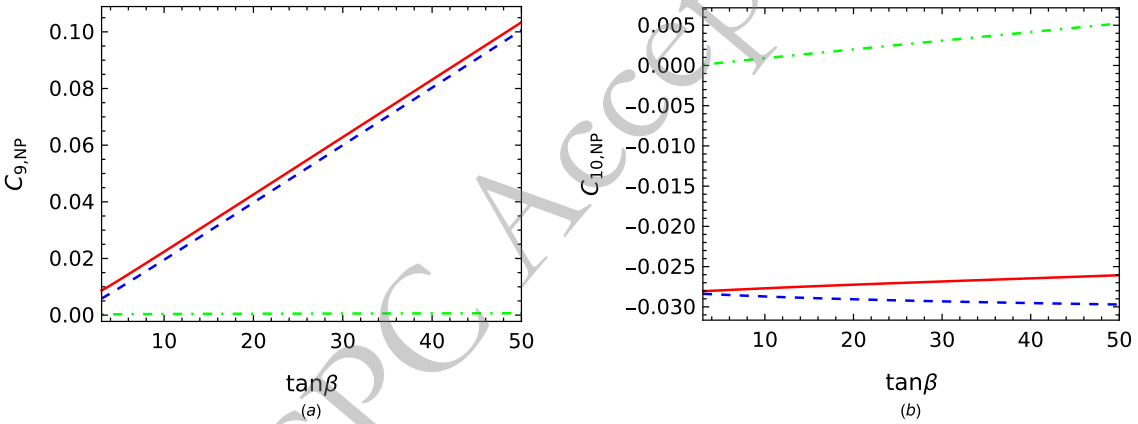

Fig. 4. (color online) Comparison of the new-physics Wilson coefficients for $\kappa = 0.4$, $A_\lambda = 0.6$ TeV, and $v_{\nu^c} = 1.8$ TeV. Panel (a) shows the full $\mu\nu$SSM result for $C_{9,\mathrm{NP}}$ (solid line), the chargino-mediated photon-penguin contribution $C^{\gamma}_{9,\chi^\pm}$ (dashed line), and the corresponding MSSM prediction (dash-dotted line). Panel (b) presents the decomposition of $C_{10,\mathrm{NP}}$, including the full $\mu\nu$SSM result (solid line), the charged-Higgs contribution (dashed line), and the chargino-mediated contribution (dash-dotted line).

CPC Accepted

tanβ dependence of the photon-penguin contribution.

The numerical dominance of the chargino-mediated photon-penguin contribution can be further understood from the different electroweak structures of the relevant penguin amplitudes. As indicated by Fig. 4(a), the close agreement between the full result and $C^{\gamma}_{9,\chi^\pm}$ suggests that the other contributions have only a limited impact on the overall result. By contrast, the charged-Higgs and neutralino-mediated Z-penguin contributions to $C_{9,\mathrm{NP}}$ are suppressed by the small leptonic vector coupling. In particular, as shown in Eq. (17), the Z-penguin contribution satisfies $C^{Z}_{9,\mathrm{NP}}(\mu_{\mathrm{EW}}) = (4s_W^2 - 1)C^{Z}_{10,\mathrm{NP}}(\mu_{\mathrm{EW}})$, where $4s_W^2 - 1 \simeq -0.08$. This relation demonstrates the suppression of the Z-penguin contribution to $C_{9,\mathrm{NP}}$ relative to its counterpart in $C_{10,\mathrm{NP}}$, further explaining why these subdominant contributions only weakly affect the total result.

Having established the origin of $C_{9,\mathrm{NP}}$, we now turn to $C_{10,\mathrm{NP}}$. For $C_{10,\mathrm{NP}}$, panel (b) shows that the total contribution exhibits only a weak dependence on tanβ, despite the different variations of the individual SUSY contributions. In particular, the charged-Higgs contribution gradually decreases with increasing tanβ, whereas the chargino contribution shows the opposite trend, leading to partial compensation between the two. Thus, their relative importance varies with tanβ, while their combined contribution remains relatively stable. The neutralino contribution is comparatively smaller than the contributions from the chargino and charged-Higgs sectors and is therefore not shown separately; however, it is included in the total result and contributes to the residual tanβ dependence. This behavior arises from the different tanβ dependences of the coupling combinations, mixing matrices, and loop functions entering the corresponding Z-penguin amplitudes, which govern the relative variations of the chargino and charged-Higgs contributions.

Although the total $C_{10,\mathrm{NP}}$ remains relatively stable over the scanned tanβ range, the relative importance of its charged-Higgs and chargino contributions can be further tuned through the flavor-mixing parameter δ^{AB}_{23}, which directly affects the magnitude of the chargino con-

tribution. For the benchmark value $\delta_{23}^{AB} = 0.6\times10^{-3}$, the charged-Higgs contribution varies only mildly, from -0.028 to -0.030, while the chargino contribution increases gradually with $\tan\beta$ (Fig. 4(b)). Varying δ_{23}^{AB} has little effect on the charged-Higgs contribution but enhances the chargino contribution throughout the scanned $\tan\beta$ range, without qualitatively changing its $\tan\beta$ dependence. Since the two contributions have opposite signs, increasing δ_{23}^{AB} enhances the relative importance of the chargino contribution and can eventually change the dominant sector. For example, for $\delta_{23}^{AB} = 0.4\times10^{-2}$ and $\upsilon_{\nu^c} = 1.8\,\text{TeV}$, the chargino and charged-Higgs contributions to $C_{10,\text{NP}}$ are approximately 0.0299 and -0.0296, respectively, at $\tan\beta \simeq 42$. As $\tan\beta$ increases further, the chargino contribution becomes dominant. Although this parameter choice can satisfy the experimental constraints from $B_s^0 \to \mu^+\mu^-$ and $\bar{B} \to X_s\gamma$ for certain ranges of $\tan\beta$, the allowed parameter space becomes strongly restricted when both constraints are imposed simultaneously. Therefore, this relatively large value of δ_{23}^{AB} is not adopted as the benchmark value in our subsequent scans.

These results demonstrate that different SUSY sectors play distinct and complementary roles in determining the semileptonic Wilson coefficients in the $\mu\nu$SSM: the chargino-mediated photon penguin primarily controls the variation of $C_{9,\text{NP}}$, whereas the interplay among the chargino, charged-Higgs, and neutralino contributions leads to the weak $\tan\beta$ dependence of $C_{10,\text{NP}}$.

Having identified the dominant origins of the semileptonic Wilson coefficients, we next analyze their impact on the physical observables of $B \to X_s l^+ l^-$.

For the chosen parameter space, we present $\text{BR}(B \to X_s l^+ l^-)$ in the low-q^2 (1–6 GeV^2) and high-q^2 (14.4–25 GeV^2) regions as functions of $\tan\beta$ in Fig. 5(a) and Fig. 5(b), respectively. The corresponding values of $A_{\text{FB}}(B \to X_s l^+ l^-)$ in the low- and high-q^2 regions are shown in Fig. 5(c) and Fig. 5(d), respectively. For brevity, we denote $\text{BR}(B \to X_s l^+ l^-)$ in the two q^2 regions as

$$\text{BR}(B \to X_s l^+ l^-)_{\text{low}} = \text{BR}(B \to X_s l^+ l^-)_{q^2\in[1,6]\,\text{GeV}^2}, \tag{47}$$

$$\text{BR}(B \to X_s l^+ l^-)_{\text{high}} = \text{BR}(B \to X_s l^+ l^-)_{q^2\in[14.4,25]\,\text{GeV}^2}. \tag{48}$$

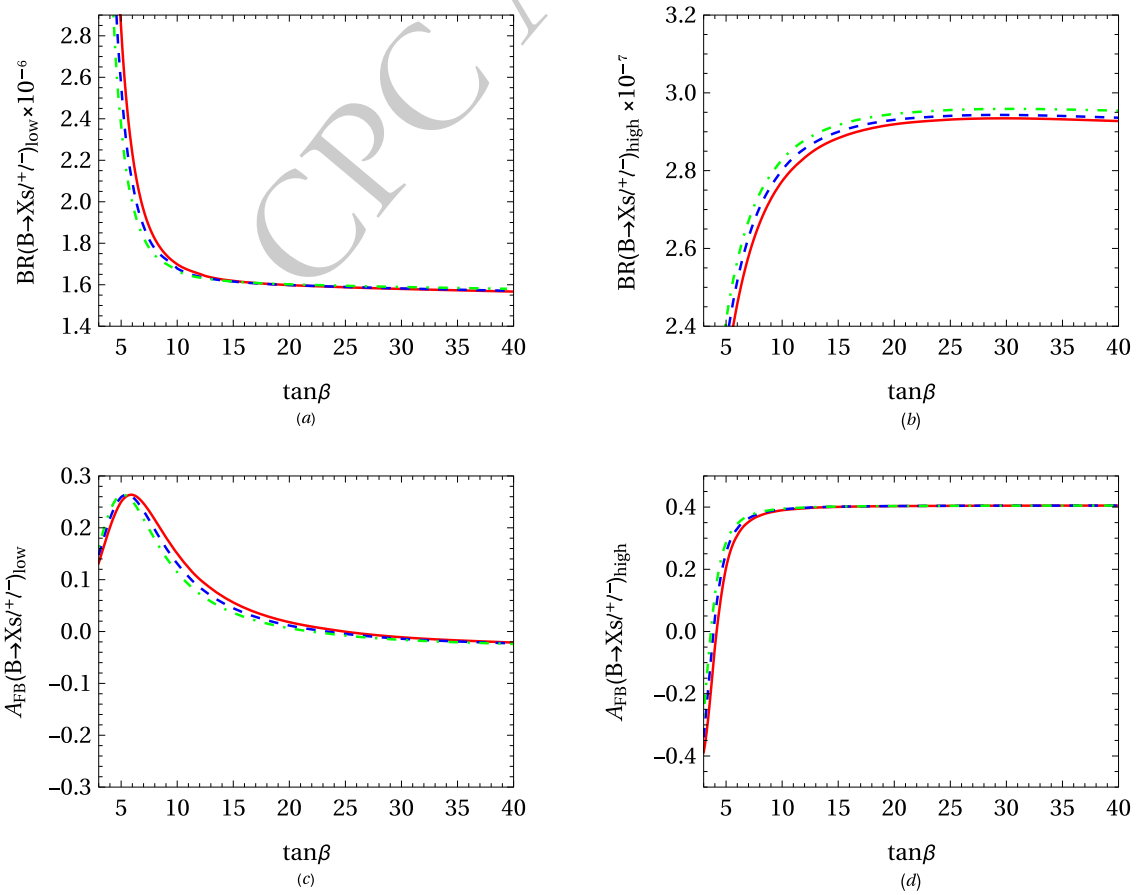

Fig. 5. (color online) (a) $\text{BR}(B \to X_s l^+ l^-)_{q^2\in[1,6]\,\text{GeV}^2}$, (b) $\text{BR}(B \to X_s l^+ l^-)_{q^2\in[14.4,25]\,\text{GeV}^2}$, (c) $A_{\text{FB}}(B \to X_s l^+ l^-)_{q^2\in[1,6]\,\text{GeV}^2}$, and (d) $A_{\text{FB}}(B \to X_s l^+ l^-)_{q^2\in[14.4,25]\,\text{GeV}^2}$ as functions of $\tan\beta$ for fixed $\kappa = 0.4$ and $A_\lambda = 0.6$ TeV, with $\upsilon_{\nu^c} = 1.8$ TeV (solid line), $\upsilon_{\nu^c} = 2.0$ TeV (dashed line), and $\upsilon_{\nu^c} = 2.2$ TeV (dash-dotted line).

CPC Accepted

The branching ratios of $B \to X_s l^+ l^-$ exhibit distinct trends in the low- and high-q^2 regions. As shown in Fig. 5(a), $\mathrm{BR}(B \to X_s l^+ l^-)_{\mathrm{low}}$ decreases gradually with increasing $\tan\beta$, while exhibiting only a mild dependence on the parameter υ_{ν^c}. The theoretical prediction for $\mathrm{BR}(B \to X_s l^+ l^-)_{\mathrm{low}}$ decreases from 2.8×10^{-6} to 1.6×10^{-6} as $\tan\beta$ increases. In contrast, Fig. 5(b) shows that $\mathrm{BR}(B \to X_s l^+ l^-)_{\mathrm{high}}$ increases from 2.3×10^{-7} to 2.9×10^{-7} as $\tan\beta$ increases. These differing trends in the two q^2 regions motivate a closer examination of the Wilson-coefficient contributions and their interplay.

To further elucidate the origin of these behaviors, we examine the relevant Wilson coefficients and their underlying particle-level contributions. Our numerical analysis shows that $\mathrm{BR}(B \to X_s l^+ l^-)_{\mathrm{low}}$ is particularly sensitive to the new-physics correction to C_7, which is dominated by the charged-Higgs contribution through γ-penguin diagrams in the $\mu\nu$SSM parameter space considered here. As discussed above, the charged-Higgs contribution to C_7 exhibits an explicit $\cot^2\beta$ dependence, as shown in Eq. (45). This dependence drives the $\tan\beta$ dependence of the low-q^2 branching fraction: as $\tan\beta$ increases from 5 to 10, C_7^{eff} changes from -1.07 to -0.28, while the branching fraction decreases from 2.83×10^{-6} to 1.70×10^{-6}, corresponding to a reduction of approximately 40%.

In contrast, $\mathrm{BR}(B \to X_s l^+ l^-)_{\mathrm{high}}$ receives contributions from C_7, C_9, and C_{10}. In the $\mu\nu$SSM parameter space considered here, the new-physics corrections to C_9 and C_{10} remain numerically subleading compared with those to C_7. Consequently, the variation in C_7 plays a more prominent role in the parameter dependence of $\mathrm{BR}(B \to X_s l^+ l^-)_{\mathrm{high}}$. As $\tan\beta$ increases from 5 to 10, the branching fraction rises from 2.28×10^{-7} to 2.77×10^{-7}, corresponding to an enhancement of approximately 21.5%. This behavior reflects the interplay among the Wilson-coefficient contributions, including partial cancellations that affect the net change in the branching fraction.

For the same $\tan\beta$ scan, different values of υ_{ν^c} lead to distinguishable variations in the observables at low $\tan\beta$, whereas their effects become less pronounced at larger $\tan\beta$. This behavior is mainly associated with the charged-Higgs sector. As shown in Eqs. (43) and (44), the charged-Higgs mass depends on both $\tan\beta$ and υ_{ν^c}, increasing from approximately 1.8 TeV to 6.2 TeV for $\upsilon_{\nu^c} = 1.8$ TeV over the scanned $\tan\beta$ range. As the charged-Higgs mass increases, its contribution to C_7 through the γ-penguin becomes increasingly suppressed, reflecting the mass dependence of the loop functions in Eq. (45). Consequently, variations in υ_{ν^c} induce smaller changes in this contribution at larger $\tan\beta$, which helps explain the weaker dependence of the observables on υ_{ν^c} in this region.

It is instructive to compare this behavior with that of $\mathrm{BR}(B_s^0 \to \mu^+\mu^-)$, which exhibits a more pronounced dependence on υ_{ν^c} than the $B \to X_s l^+ l^-$ observables, as shown in Fig. 3. This difference can be traced to the dependence of the chargino sector on the effective μ parameter, $\mu = 3\lambda\upsilon_{\nu^c}$. Varying υ_{ν^c} modifies the chargino mass matrix and mixing, thereby changing the interaction vertices that contribute to the scalar Wilson coefficient C_S. The resulting variation in C_S accounts for the stronger υ_{ν^c} dependence of $\mathrm{BR}(B_s^0 \to \mu^+\mu^-)$.

By comparison, the forward-backward asymmetries exhibit a different pattern. We define $A_{\mathrm{FB}}(B \to X_s l^+ l^-)$ in the two q^2 regions as

$$A_{\mathrm{FB}}(B \to X_s l^+ l^-)_{\mathrm{low}} = A_{\mathrm{FB}}(B \to X_s l^+ l^-)_{q^2\in[1,6]\,\mathrm{GeV}^2}, \tag{49}$$

$$A_{\mathrm{FB}}(B \to X_s l^+ l^-)_{\mathrm{high}} = A_{\mathrm{FB}}(B \to X_s l^+ l^-)_{q^2\in[14.4,25]\,\mathrm{GeV}^2}. \tag{50}$$

Figures 5(c) and Fig. 5(d) show that $A_{\mathrm{FB}}(B \to X_s l^+ l^-)_{\mathrm{low}}$ initially increases and then decreases as $\tan\beta$ increases, whereas $A_{\mathrm{FB}}(B \to X_s l^+ l^-)_{\mathrm{high}}$ generally increases. Specifically, the low-q^2 asymmetry varies from -0.02 to 0.26, while the high-q^2 asymmetry increases from -0.4 to 0.4 over the considered range of $\tan\beta$. To clarify the origin of these distinct behaviors, we examine the analytical structure of A_{FB} and investigate the $\tan\beta$ dependence of its dominant contributions.

As shown in Eq. (32), the forward-backward asymmetry A_{FB} for $B \to X_s l^+ l^-$ is given by the ratio of $\bar{A}_{\mathrm{FB}}$ to $R(q^2)$. As shown in Eq. (31), $\bar{A}_{\mathrm{FB}}$ receives contributions from four interference structures: C_7C_{10}, C_9C_{10}, C_7C_S, and C_9C_S. The first two are dominant in our analysis. In the low-q^2 region, the contributions proportional to C_7C_S and C_9C_S are numerically negligible. We therefore focus on the individual contributions of the C_7C_{10} and C_9C_{10} interference terms to A_{FB} and their dependence on $\tan\beta$. To illustrate their relative importance, Fig. 6(a) compares the total $A_{\mathrm{FB}}(B \to X_s l^+ l^-)_{\mathrm{low}}$ with the individual contributions from the C_7C_{10} and C_9C_{10} interference terms. For $\tan\beta < 5.5$, the total asymmetry is primarily governed by the C_7C_{10} contribution, whereas the shifted peak reflects the interplay and partial cancellation between the two dominant interference contributions. As $\tan\beta$ increases into the range $5.5 < \tan\beta < 7$, the relative importance of the two contributions changes, and the C_9C_{10} term becomes increasingly significant. For $\tan\beta > 7$, the C_7C_{10} contribution becomes dominant again. Throughout the considered $\tan\beta$ range, the combined C_7C_{10} and C_9C_{10} contributions reproduce the total $A_{\mathrm{FB}}(B \to X_s l^+ l^-)_{\mathrm{low}}$, confirming their quantitative dominance in the low-q^2 region.

A similar decomposition is performed for the high-q^2 region, where the dominant interference contribution changes at a different value of $\tan\beta$ because of the dis-

CPC Accepted

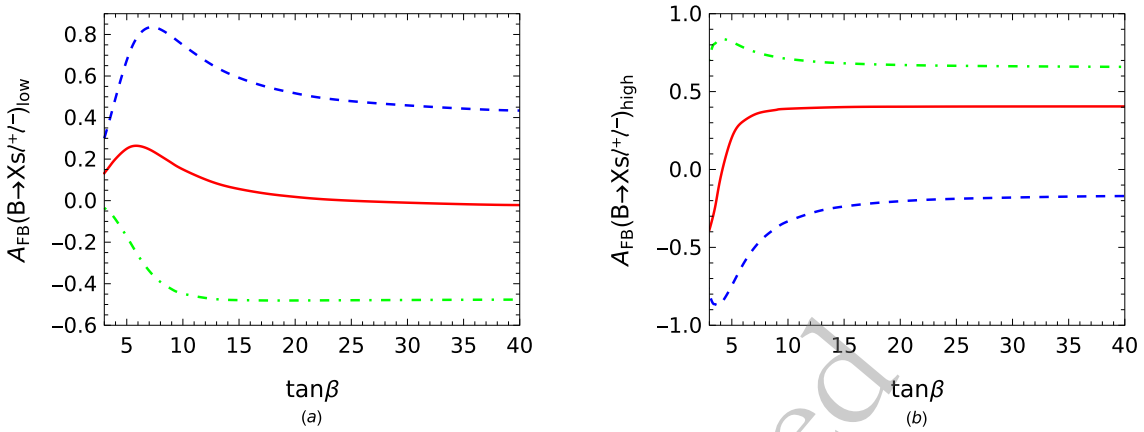

Fig. 6. (color online) Decomposition of (a) $A_{\rm FB}(B\to X_s l^+l^-)_{\rm low}$ and (b) $A_{\rm FB}(B\to X_s l^+l^-)_{\rm high}$. The total $A_{\rm FB}$ is shown as a solid line, the C_7C_{10} interference as a dashed line, and the C_9C_{10} interference as a dash-dotted line.

tinct q^2 dependence. As shown in Fig. 6(b), for $\tan\beta < 10$, the total $A_{\rm FB}(B\to X_s l^+l^-)_{\rm high}$ follows the behavior of the C_7C_{10} contribution. As $\tan\beta$ increases beyond 10, the C_9C_{10} contribution becomes increasingly significant and eventually dominates. The combined C_7C_{10} and C_9C_{10} contributions closely reproduce the total high-q^2 asymmetry throughout the considered parameter range, confirming that these two interference structures provide the dominant contributions.

To further understand the behavior of the C_7C_{10} contribution shown in Fig. 6(a), we examine the normalized interference term $C_7C_{10}/R(q^2)$ in the low-q^2 region. As shown in Table 4, when $\tan\beta$ increases from 3 to 5, C_7C_{10} decreases by approximately 55%, from 12.52 to 5.66, whereas $R(q^2)$ decreases by approximately 80%, from 0.005 to 0.001. The larger relative decrease in $R(q^2)$ increases the normalized term from 0.25×10^4 to 0.57×10^4. At larger $\tan\beta$, $R(q^2)$ approaches a plateau, whereas C_7C_{10} continues to decrease. Consequently, the normalized term declines to 0.35×10^4 at $\tan\beta = 40$. These results show that the peak structure of the C_7C_{10}-only contribution in Fig. 6(a) arises from the competition between the decreasing numerator and the changing normalization factor.

In contrast to the C_7C_{10} contribution, the C_9C_{10} term varies only mildly, changing from -17.37 at $\tan\beta = 3$ to -16.97 at $\tan\beta = 40$, corresponding to an approximately 2.3% reduction in magnitude. Meanwhile, $R(q^2)$ decreases from 0.005 to 0.000358 over the same interval. As shown in Table 4, the normalized term $C_9C_{10}/R(q^2)$ therefore becomes substantially more negative, changing from -0.35×10^4 to -4.74×10^4. This indicates that the evolution of the normalized interference term is driven primarily by the decrease in $R(q^2)$ rather than by a substantial change in the C_9C_{10} term itself. At large $\tan\beta$, $R(q^2)$ stabilizes, and the ratio gradually approaches a plateau, consistent with the behavior of the C_9C_{10}-only contribution in Fig. 6(a). The contrasting behaviors of the two normalized interference terms modify their relative contributions to the full $A_{\rm FB}$.

The non-monotonic behavior of the full $A_{\rm FB}$ in the low-q^2 region therefore arises from the interplay between the two dominant normalized interference terms, $C_7C_{10}/R(q^2)$ and $C_9C_{10}/R(q^2)$, whose different $\tan\beta$ dependences shape the overall behavior of the asymmetry. A similar analysis can be applied to the high-q^2 region, where the relative importance of the two interference contributions evolves differently, as shown in Fig. 6(b), accounting for the overall increasing trend of $A_{\rm FB}(B\to X_s l^+l^-)_{\rm high}$.

Building on the preceding analysis of the $\tan\beta$ scan, we further examine the dependence of the $B\to X_s l^+l^-$ ob-

Table 4. Numerical contributions to $A_{\rm FB}$ from the dominant interference terms and their dependence on $\tan\beta$, evaluated in the low-q^2 region.

Quantity	$\tan\beta = 3$	$\tan\beta = 5$	$\tan\beta = 20$	$\tan\beta = 40$	Trend
C_7C_{10}	12.52	5.66	1.54	1.27	Monotonically decreasing
C_9C_{10}	−17.37	−17.31	−17.19	−16.97	Slowly increasing
$R(q^2)\times10^3$	5.00	1.00	0.359	0.358	Decreases and then plateaus
$(C_7C_{10}/R(q^2))\times10^{-4}$	0.25	0.57	0.43	0.35	Increases and then decreases
$(C_9C_{10}/R(q^2))\times10^{-4}$	−0.35	−1.73	−4.78	−4.74	More negative, then plateaus

CPC Accepted

servables on κ to determine whether the same physical mechanisms remain dominant. Fig. 7 presents the branching ratio $\mathrm{BR}(B \to X_s l^+ l^-)$ and the forward-backward asymmetry $A_{\mathrm{FB}}(B \to X_s l^+ l^-)$ as functions of κ for fixed $\tan\beta = 25$, with parameter points satisfying the experimental constraints from $\bar{B} \to X_s\gamma$ and $B_s^0 \to \mu^+\mu^-$ shown in Fig. 8.

Fig. 7 shows that the branching ratios are more sensitive to κ for smaller A_λ. For $A_\lambda = 0.05\,\mathrm{TeV}$, as κ increases from 0.01 to 0.6, the charged-Higgs mass rises from approximately 1.2 TeV to 5.0 TeV. Over this interval, $\mathrm{BR}(B \to X_s l^+ l^-)_{\mathrm{low}}$ decreases by approximately 11%, from 1.8×10^{-6} to 1.61×10^{-6}, whereas $\mathrm{BR}(B \to X_s l^+ l^-)_{\mathrm{high}}$ increases by approximately 11%, from 2.69×10^{-7} to 2.98×10^{-7}. For $A_\lambda = 0.2\,\mathrm{TeV}$, the charged-Higgs mass varies from approximately 2.3 TeV to 5.1 TeV over the same κ range. The corresponding changes in $\mathrm{BR}(B \to X_s l^+ l^-)_{\mathrm{low}}$ and $\mathrm{BR}(B \to X_s l^+ l^-)_{\mathrm{high}}$ are much smaller, amounting to a 2.4% decrease and a 3.8% increase, respectively. This quantitative comparison demonstrates that larger A_λ weakens the sensitivity of both branching ratios to κ.

This behavior is primarily associated with the charged-Higgs contributions to the Wilson coefficients. As shown in Eqs. (43) and (44), variations in κ and A_λ modify the charged-Higgs mass, thereby affecting the corresponding loop contributions to the relevant Wilson coefficients.

Overall, variations in κ mainly affect the magnitudes of the observables without qualitatively altering the dominant physical mechanisms. The forward-backward asymmetry $A_{\mathrm{FB}}(B \to X_s l^+ l^-)$ exhibits a similar dependence on κ. Unlike in the $\tan\beta$ scan, where the relative importance of the normalized C_7C_{10} and C_9C_{10} interference contributions changes as $\tan\beta$ increases, the κ scan does not produce a comparable qualitative change in their relative importance. This behavior can be understood from the fact that κ primarily affects the Higgs-sector spectrum and the magnitudes of the loop contributions, while the relative structure of the Wilson coefficients remains qualitatively stable. Consequently, the C_7C_{10} and C_9C_{10} interference terms remain the dominant contributions to A_{FB}, although their relative weights may vary with κ.

CPC Accepted

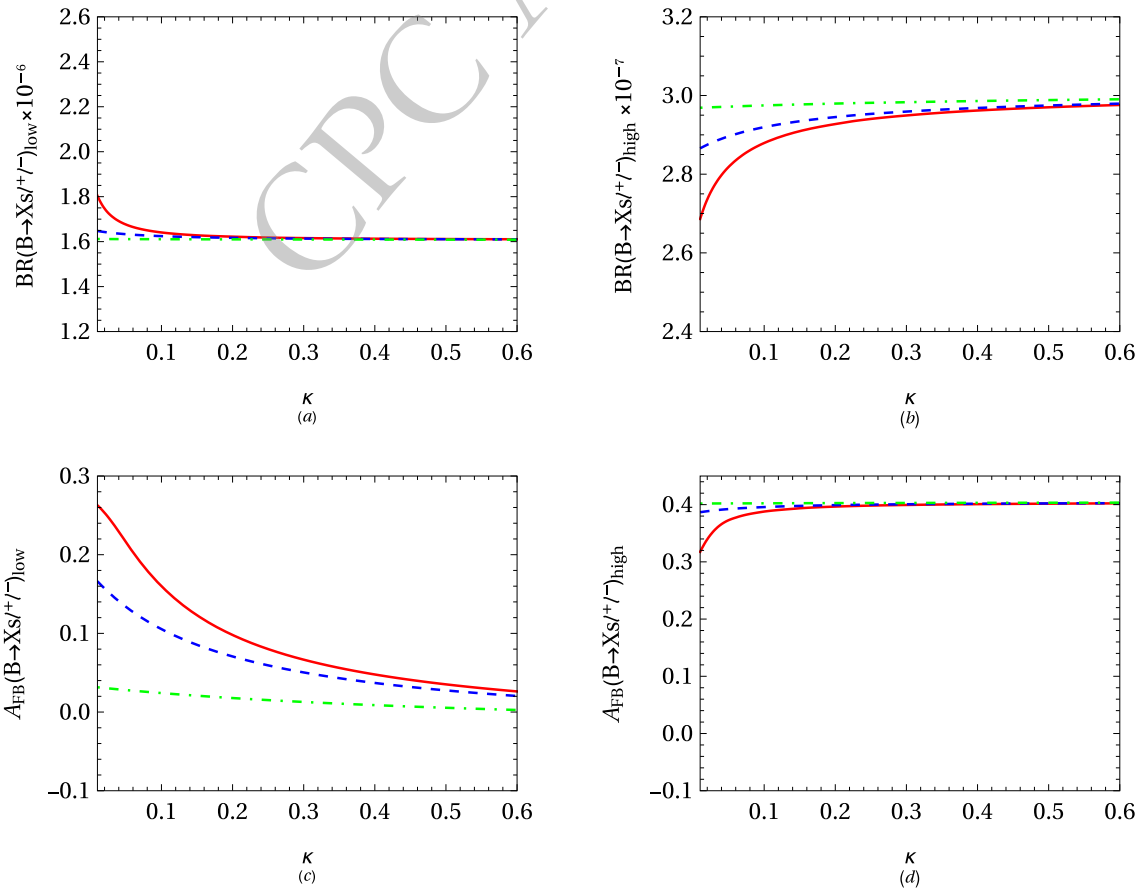

Fig. 7. (color online) (a) $\mathrm{BR}(B \to X_s l^+ l^-)_{q^2\in[1,6]\,\mathrm{GeV}^2}$, (b) $\mathrm{BR}(B \to X_s l^+ l^-)_{q^2\in[14.4,25]\,\mathrm{GeV}^2}$, (c) $A_{\mathrm{FB}}(B \to X_s l^+ l^-)_{q^2\in[1,6]\,\mathrm{GeV}^2}$, and (d) $A_{\mathrm{FB}}(B \to X_s l^+ l^-)_{q^2\in[14.4,25]\,\mathrm{GeV}^2}$ as functions of κ for fixed $\tan\beta = 25$ and $\upsilon_{\nu^c} = 2.0$ TeV, with $A_\lambda = 0.05$ TeV (solid line), $A_\lambda = 0.2$ TeV (dashed line), and $A_\lambda = 1$ TeV (dash-dotted line).

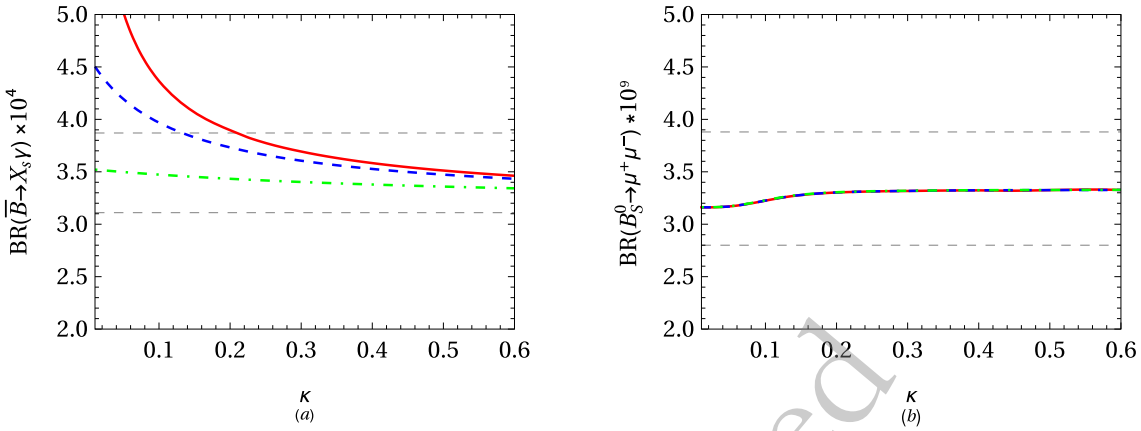

Fig. 8. (color online) For fixed $\tan\beta = 25$ and $v_{\nu^c} = 2.0$ TeV, (a) BR($\bar{B} \to X_s\gamma$) and (b) BR($B_s^0 \to \mu^+\mu^-$) are shown as functions of κ for $A_\lambda = 0.05$ TeV (solid line), $A_\lambda = 0.2$ TeV (dashed line), and $A_\lambda = 1$ TeV (dash-dotted line).

VI. DISCUSSION ON ADDITIONAL CONSTRAINTS

Although this work primarily focuses on the underlying mechanisms of the $b \to s$ transitions within the $\mu\nu$SSM framework, it is important to ensure that the adopted parameter regions are consistent with other low-energy observables. We therefore briefly discuss several additional phenomenological constraints relevant to the present R-parity-violating scenario.

The $\mu\nu$SSM can induce additional contributions to B_s–$\bar{B}_s$ mixing through chargino-, neutralino-, and scalar-mediated loop diagrams. However, unlike generic trilinear RPV scenarios, the origin of R-parity violation in the $\mu\nu$SSM is closely related to the final three terms in the superpotential (Eq. (5)),

$$W \supset Y^{\nu}_{ij}\hat{H}_u\hat{L}_i\hat{\nu}^c_j + \lambda_i\hat{\nu}^c_i\hat{H}_d\hat{H}_u + \frac{1}{3}\kappa_{ijk}\hat{\nu}^c_i\hat{\nu}^c_j\hat{\nu}^c_k. \tag{51}$$

In the present analysis, the neutrino Yukawa couplings Y^{ν}_{ij} are negligibly small and are set to zero in the numerical evaluation. The corresponding left-handed sneutrino vacuum expectation values are likewise negligible. The λ_i and κ_{ijk} interactions primarily affect the singlet-sneutrino, Higgsino, chargino, and neutralino sectors, rather than directly generating sizable flavor-changing interactions in the quark sector. Consequently, their effects on B_s–$\bar{B}_s$ mixing arise only indirectly through loop corrections. A dedicated numerical analysis of B_s–$\bar{B}_s$ mixing, including the relevant box-diagram contributions, is beyond the scope of the present work.

Exclusive $B \to K^*\mu^+\mu^-$ and $B \to K^*\nu\bar{\nu}$ observables also provide important constraints on the relevant Wilson coefficients. Within the parameter space considered in this work, the predicted branching ratios and forward-backward asymmetries are consistent with current experimental data. A more detailed study of these observables in the $\mu\nu$SSM framework will be presented elsewhere.

Recent global analyses of $b \to s$ transitions [76–79] have identified allowed regions in the space of the new-physics Wilson coefficients $C_{7,\mathrm{NP}}$, $C_{9,\mathrm{NP}}$, and $C_{10,\mathrm{NP}}$ that are consistent with current experimental data. Within the allowed parameter space of the present work, the new-physics contributions of the $\mu\nu$SSM to the relevant Wilson coefficients remain consistent with the experimentally measured branching ratio of $B \to X_s\mu^+\mu^-$. They also lie within the corresponding 68% confidence-level preferred regions reported in Ref. [76].

VII. SUMMARY

In this paper, we investigate the branching ratios and forward-backward asymmetries of the rare inclusive decay $B \to X_s l^+ l^-$ in the $\mu\nu$SSM, accounting for experimental constraints from $\bar{B} \to X_s\gamma$, $B_s^0 \to \mu^+\mu^-$, and the mass of the 125 GeV SM-like Higgs boson. We systematically analyze new-physics corrections to the relevant flavor-changing Wilson coefficients and clarify the dominant particle sectors responsible for these effects. The extended fermion and scalar sectors of the $\mu\nu$SSM induce characteristic modifications through altered coupling and mixing structures, leading to nontrivial corrections to the B-meson decay observables.

A systematic decomposition of the interference contributions to the forward-backward asymmetry reveals that the C_7C_{10} and C_9C_{10} interference terms dominate its phenomenological behavior in both the low- and high-q^2 regions. Their competition accounts for the distinct parametric dependences in the two kinematic regimes.

Further analysis of the parameter dependences of the Wilson coefficients shows that the low-q^2 branching ratio is primarily governed by the charged-Higgs-induced correction to C_7. In contrast, the chargino sector dominates the new-physics photon-penguin contribution to

CPC Accepted

$C_{9,\mathrm{NP}}$, whereas the $C_{10,\mathrm{NP}}$ correction arises from partial cancellation between the charged-Higgs and chargino contributions. Variations in υ_{ν^c}, κ, and A_λ mainly modify the magnitude of the new-physics effects by altering the Higgs-sector spectrum, without changing the dominant physical mechanisms identified in this analysis.

References

[1] B. Grinstein, M.J. Savage and M.B. Wise Nucl. Phys. B319 (1989) 271.
[2] M. Misiak, Nucl. Phys. B**393**(1993)23[Erratum-ibid. B**439**(1995)461].
[3] A. J. Buras, M. Münz, Phys. Rev. D **52**, 186 (1995)
[4] N. G. Deshpande, J. Trampetic, K. Panose, Phys. Rev. D **39**, 1461 (1989)
[5] C. S. Lim, T. Morozumi, A. I. Sanda, Phys. Lett. B **218**, 343 (1989)
[6] P. J. O'Donnell, H.K.K. Tung, Phys. Rev. D **43**, 2067 (1991)
[7] T. Huber, T. Hurth, J. Jenkins, E. Lunghi, Q. Qin *et al.*, JHEP **11** (2024) 130 [arXiv: 2404.03517]. [Erratum: JHEP **05** (2025) 099].
[8] B. Aubert *et al.*, BABAR collaboration, Phys. Rev. Lett. **93**, 081802 (2004)
[9] J. P. Lees *et al.* [BaBar Collaboration], Phys. Rev. Lett. **112**, 211802 (2014)
[10] M. Iwasaki *et al.*, Phys. Rev. D **72**, 092005 (2005)
[11] Y. Sato *et al.*, BELLE collaboration, Phys. Rev. D**93**(2016)032008; *ibid.***93**(2016)059901.
[12] A. Ghinculov, T. Hurth, G. Isidori, and Y. P. Yao, Eur. Phys. J. C **33**, S288 (2004), arXiv: hep-ph/0310187[hep-ph]
[13] A. Ali, G. F. Giudice, and T. Mannel, Z. Phys. C **67**, 417 (1995), arXiv: hep-ph/9408213[hep-ph]
[14] T. Huber, T. Hurth, J. Jenkins, E. Lunghi, Q. Qin, and K. K. Vos, JHEP **10**, 088 (2020), arXiv: 2007.04191[hep-ph]
[15] Z. Ligeti and F. J. Tackmann, Phys. Lett. B **653**, 404 (2007), arXiv: 0707.1694[hep-ph]
[16] A. Ghinculov, T. Hurth, G. Isidori, and Y. P. Yao, Nucl. Phys. B **685**, 351 (2004), arXiv: hep-ph/0312128[hep-ph]
[17] S. Fukae, C. S. Kim, T. Morozumi and T. Yoshikawa, Phys. Rev. D**59**(1999)074013; A. Ali, E. Lunghi, C. Greub, and G. Hiller, Phys. Rev. D**66**(2002)034002.
[18] S. Bertolini, F. Borzumati, A. Masiero and G. Ridolfi, Nucl. Phys. B **353**, 591 (1991)
[19] J. L. Hewett, Phys. Rev. Lett. **70**, 1045 (1993), arXiv: hep-ph/9211256
[20] P. Ciafaloni, A. Romanino and A. Strumia, Nucl. Phys. B **524**, 361 (1998)
[21] M. Ciuchini, G. Degrassi, P. Gambino and G. F. Giudice, Nucl. Phys. B **527**, 21 (1998)
[22] F. M. Borzumati and C. Greub, Phys. Rev. D **58**, 074004 (1998)
[23] F. Borzumati, C. Greub, T. Hurth and D. Wyler, Phys. Rev. D **62**, 075005 (2000)
[24] X. G. He, T. D. Nguyen and R. R. Volkas, Phys. Rev. D **38**, 814 (1988)
[25] W. Skiba and J. Kalinowski, Nucl. Phys. B **404**, 3 (1993)
[26] S. R. Choudhury and N. Gaur, Phys. Lett. B **451**, 86 (1999), arXiv: hep-ph/9810307
[27] C. S. Huang, W. Liao, Q. S. Yan and S. H. Zhu, Phys. Rev. D **63**, 114021 (2001) [Erratum-ibid. D **64**, 059902 (2001)] [hep-ph/0006250].
[28] P. Cho, M. Misiak and D. Wyler, Phys. Rev. **D54**, 3329 (1996)
[29] T.-F. Feng, Y.-L. Yan, H.-B. Zhang and S.-M. Zhao, Int. J. Mod. Phys. A **31**, 1650092 (2016), arXiv: 1603.07578[hep-ph]
[30] T.-F. Feng, J.-L. Yang, H.-B. Zhang, S.-M. Zhao and R.-F. Zhu, Phys. Rev. D **94**, 115034 (2016), arXiv: 1612.02094[hep-ph]
[31] J. L. Yang, T. F. Feng, S. M. Zhao, R. F. Zhu, X. Y. Yang and H. B. Zhang, Eur. Phys. J. C **78**(9), 714 (2018), arXiv: 1803.09904[hep-ph]
[32] R. Barbieri and G. F. Giudice, Phys. Lett. B **309**, 86 (1993)
[33] A. Shaw, Phys. Rev. D **99**, 115030 (2019), arXiv: 1903.10302
[34] A. Ali, P. Ball, L. T. Handoko and G. Hiller, Phys. Rev. D **61**, 074024 (2000), arXiv: hep-ph/9910221
[35] A. Masiero and L. Silvestrini, B Physics and CP Violation, Honolulu, p. 172, (1997) [arXiv: hep-ph/9709244].
[36] A. Masiero and L. Silvestrini, Highlights of Subnuclear Physics, Erice, p. 404, (1997) [arXiv: hep-ph/9711401].
[37] E. Lunghi, A. Masiero, I. Scimemi and L. Silvestrini, Nucl. Phys. B **568**, 120 (2000), arXiv: hep-ph/9906286
[38] Z. J. Xiao, F. G. Li and W. J. Zou, Commun. Theor. Phys. **46**, 687 (2006)
[39] H. E. Haber, G. L. Kane, Phys. Rept. **117**, 75 (1985)
[40] J. Rosiek, Phys. Rev. D **41**, 3464 (1990)
[41] D. E. López-Fogliani, C. Muñoz, Phys. Rev. Lett. **97**, 041801 (2006)
[42] N. Escudero, D. E. López-Fogliani, C. Muñoz, R. Ruiz de Austri, JHEP **12**, 099 (2008)
[43] J. Fidalgo, D. E. López-Fogliani, C. Muñoz, R. Ruiz de Austri, JHEP **10**, 020 (2011)
[44] J. E. Kim, H. P. Nilles, Phys. Lett. B **138**, 150 (1984)
[45] H.-B. Zhang, T.-F. Feng, L.-N. Kou and S.-M. Zhao, Int. J. Mod. Phys. A **28**, 1350117 (2013), arXiv: 1307.6284
[46] H.-B. Zhang, G.-H. Luo, T.-F. Feng, S.-M. Zhao, T.-J. Gao and K.-S. Sun, Mod. Phys. Lett. A **29**, 1450196 (2014), arXiv: 1409.6837[hep-ph]
[47] K. K. Meng, H. B. Zhang and J. L. Yang, Phys. Rev. D **111**, 035036 (2025), arXiv: 2502.05466[hep-ph]
[48] H.-B. Zhang, T.-F. Feng, G.-F. Luo, Z.-F. Ge and S.-M. Zhao, JHEP 07 (2013) 069 [Erratum ibid. JHEP 10 (2013) 173].
[49] H.-B. Zhang, T.-F. Feng, S.-M. Zhao, Fei Sun, Int. J. Mod. Phys. A **29**, 1450123 (2014)
[50] H.-B. Zhang, T.-F. Feng, F. Sun, K.-S. Sun, J.-B. Chen and S.-M. Zhao, Phys. Rev. D **89**, 115007 (2014)
[51] R.Grigjanis, P. J. ODonnell, M. Sutherland and H. Navelet, Phys. Rep. **22**, 93 (1993)
[52] G. Buchalla, A. J. Buras and M. E. Lautenbacher, Rev. Mod. Phys. **68**, 1125 (1996)
[53] L. Lin, T. F. Feng and F. Sun, Mod. Phys. Lett. A **24**, 2181 (2009)
[54] X. Y. Yang and T. F. Feng, JHEP **1005**, 059 (2010)
[55] P. Goertz and T. Pfoh, Phys. Rev. D **84**, 095016 (2011)
[56] A. J. Buras, M. Misiak, M. Munz and S. Pokorski, Nucl. Phys. B **424**, 374 (1994)

CC Accepted

[57] W. Altmannshofer, P. Ball, A. Bharucha, A. J. Buras, D. M. Straub, and M. Wick, JHEP **0901**, 019 (2009), arXiv: 0811.1214[hep-ph]
[58] P. Gambino, M. Gorbahn and U. Haisch, Nucl. Phys. B **673**, 238 (2003)
[59] Y. B. Dai, C. S. Huang and H. W. Huang, Phys. Lett. B **390**, 257 (1997) [Erratum-ibid. B **513**, 429 (2001)] [arXiv: hep-ph/9607389].
[60] I. Scimemi, Nucl. Phys. B, Proc. Suppl. **81**, 219 (2000), arXiv: hep-ph/9911355
[61] G. D'Ambrosio, G.F. Giudice, G.Isidori, A.Strumia, *Nucl. Phys.* B **645**, 155 (2002)
[62] S. Navas *et al*. [Particle Data Group], Phys. Rev. D **110**, 030001 (2024)
[63] ATLAS Collaboration, Phys. Rev. D **87**, 012008 (2013)
[64] CMS Collaboration, JHEP **1210**, 018 (2012)
[65] G. Aad *et al*. (ATLAS), Eur. Phys. J. C **81**(11), 1023 (2021), arXiv: 2106.09609
[66] Y. S. Amhis *et al*. [HFLAV], Phys. Rev. D **107**(5), 052008 (2023), arXiv: 2206.07501[hep-ex]
[67] M. Aaboud *et al*. [ATLAS], JHEP **04**, 098 (2019), arXiv: 1812.03017[hep-ex]
[68] A. M. Sirunyan *et al*. [CMS], JHEP **04**, 188 (2020), arXiv: 1910.12127[hep-ex]
[69] R. Aaij *et al*. [LHCb], Phys. Rev. Lett. **128**(4), 041801 (2022), arXiv: 2108.09284[hep-ex]
[70] A. Tumasyan *et al*. [CMS], Phys. Lett. B **842**, 137955 (2023), arXiv: 2212.10311[hep-ex]
[71] M. Misiak, A. Rehman and M. Steinhauser, JHEP **06**, 175 (2020), arXiv: 2002.01548[hep-ph]
[72] M. Beneke, C. Bobeth and R. Szafron, Phys. Rev. Lett. **120**(1), 011801 (2018), arXiv: 1708.09152[hep-ph]
[73] M. Beneke, C. Bobeth and R. Szafron, JHEP **10**, 232 (2019) [erratum: JHEP **11**, 099 (2022)] [arXiv: 1908.07011 [hep-ph]].
[74] M. Czaja and M. Misiak, Ratio, Symmetry **16**(7), 917 (2024), arXiv: 2407.03810[hep-ph]
[75] T. Hurth, G. Isidori, J. F. Kamenik, and F. Mescia, Nucl. Phys. B **808**, 326 (2009), arXiv: 0807.5039[hep-ph]
[76] T. Hurth, F. Mahmoudi, and S. Neshatpour, JHEP **12**, 053 (2014), arXiv: 1410.4545[hep-ph]
[77] W. Altmannshofer and D. M. Straub, Eur. Phys. J. C **75**(8), 382 (2015), arXiv: 1411.3161[hep-ph]
[78] J. Aebischer, J. Kumar, P. Stangl, and D. M. Straub, Eur. Phys. J. C **79**(6), 509 (2019), arXiv: 1810.07698[hep-ph]
[79] M. Alguer, B. Capdevila, S. Descotes-Genon, J. Matias, and M. Novoa-Brunet, Eur. Phys. J. C **82**(4), 326 (2022), arXiv: 2104.08921[hep-ph]

CPC Accepted